

Electrorheological Fluids: Mechanisms, Dynamics, and Microfluidics Applications

Ping Sheng and Weijia Wen

Department of Physics, Hong Kong University of Science and Technology, Clear Water Bay, Kowloon, Hong Kong, China; email: sheng@ust.hk, phwen@ust.hk

Annu. Rev. Fluid Mech. 2012. 44:143–74

First published online as a Review in Advance on September 19, 2011

The *Annual Review of Fluid Mechanics* is online at fluid.annualreviews.org

This article's doi:
10.1146/annurev-fluid-120710-101024

Copyright © 2012 by Annual Reviews.
All rights reserved

0066-4189/12/0115-0143\$20.00

Keywords

induced polarization, variational effective dielectric constant formulation, giant electrorheological fluids, aligned dipolar filaments, electrorheological fluid dynamics, microfluidic logic gate

Abstract

Electrorheological (ER) fluids, consisting of solid particles dispersed in an insulating liquid, display the special characteristic of electric-field-induced rheological variations. Nearly six decades after their discovery, ER fluids have emerged as materials of increasing scientific fascination and practical importance. This review traces the mechanisms responsible for these fluids' ER response and their attendant theoretical underpinnings. In particular, ER fluids are divided into two different types, dielectric electrorheological (DER) and giant electrorheological (GER), which reflect the underlying electric susceptibility arising from the induced dielectric polarization and the orientational polarization of molecular dipoles, respectively. The formulation of a continuum ER hydrodynamics is described in some detail. As an electric-mechanical interface, ER fluids have broad application potential in electrifying the control of mechanical devices. This review focuses on their applications in microfluidic chips, in which GER fluids have enabled a variety of digitally controlled functionalities.

1. INTRODUCTION

Electrorheological (ER) fluids are a type of colloid whose rheological characteristics can be altered upon the application of an electric field. Such rheological variation is generally reversible and occurs within 10 ms. ER fluids can serve as an electric-mechanical interface, and when they are coupled with sensors (as triggers to activate the electric field), many mechanical devices such as clutches, valves, and dampers may be converted into active mechanical elements capable of responding to environmental variations. Hence ER fluids are sometimes denoted as a type of smart fluid. The diverse application potential has made ER fluids a persistent topic of study ever since their discovery over six decades ago by Winslow (1949). Initially treated as a subject of scientific curiosity, the ER effect and the attendant search for better ER materials attracted serious research efforts beginning in the late 1980s, fueled undoubtedly in part by their envisioned applications (Klingenberg et al. 1989; Chen et al. 1991, 1992; Tao & Sun 1991; Davis 1992a,b; Halsey 1992; Bullough 1996). In particular, there has been extensive research into the basic mechanisms of the ER effect (Chen & Conrad 1994, Ma et al. 1996, Tam et al. 1997, Wen et al. 1999, Choi et al. 2001). The more recent discovery of the giant electrorheological (GER) effect (Wen et al. 2003, 2004; Huang et al. 2006), together with its appeal in the basic science of nanoparticles and their dynamics, has provided a new direction in this area. The strong electrical response of GER fluids has been particularly useful in a diverse array of functionalities in microfluidic chips (Nakano et al. 2002; Yoshida et al. 2002; Liu et al. 2006a,b; Niu et al. 2005, 2006a,b, 2007, 2009; Wang et al. 2010).

1.1. Heuristic Understanding of the Electrorheological Effect

Let us consider a dispersion of particles in a fluid medium. Both the particles and the fluid are electrically nonconducting or only slightly conducting, so as to avoid electrical breakdown under a moderate electrical field. When an electric field \vec{E} is applied to such a colloidal dispersion, the particles will be electrically polarized, owing to the difference in the dielectric constant of the solid and that of the fluid. If ε_s denotes the complex dielectric constant of the solid particles and ε_ℓ that of the liquid, then for a sphere with radius R , the induced dipole moment may be expressed as

$$\vec{p} = \frac{\varepsilon_s - \varepsilon_\ell}{\varepsilon_s + 2\varepsilon_\ell} R^3 \vec{E}_l = \beta R^3 \vec{E}_l. \quad (1)$$

Here β is the Claussius-Mossotti (CM) factor, and \vec{E}_l should be understood as the field at the location of the particle, i.e., the local field. The resulting (induced) dipole-dipole interaction between the particles implies that the random dispersion is not the lowest energy state of the system, and particles would tend to aggregate and form chains/columns along the applied field direction (**Figure 1**). The formation of chains/columns is the reason why such colloids exhibit an increased viscosity or even solid-like behavior when sheared in a direction perpendicular to the electric field. However, the formation of chains/columns is governed by the competition between electrical energy and the Brownian motion of the particles, manifest in the value of the dimensionless parameter $\gamma = \vec{p} \cdot \vec{E} / k_B T$, where k_B is the Boltzmann constant and T is the temperature. For room temperature and \vec{p} given by Equation 1, $\gamma > 1$ defines the ER regime. Thus for $\beta^{1/3} R \sim 100$ nm, the field should be larger than 2 kV cm^{-1} for the system to be in the ER regime.

1.2. Two Types of Electrorheological Fluids

Electric polarization of a collection of atoms/molecules can arise in two ways from an applied electric field. One is the induced polarization process that underlies the traditional ER effect,

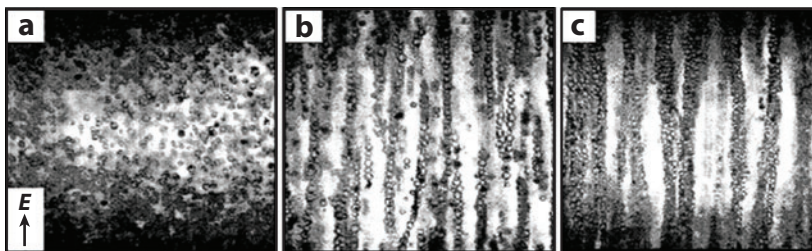


Figure 1

The structural evolution of dielectric microspheres under an increasing electric field, from (a) no field, to (b) a moderate field of 500 V mm^{-1} , to (c) a strong field of 900 V mm^{-1} . Here the electrorheological fluid consists of $1.5\text{-}\mu\text{m}$ glass spheres suspended in silicone oil. Figure adapted from Wen et al. (2007).

described heuristically above. We denote this type as the dielectric electrorheological (DER) effect. The other is by aligning the initially randomly oriented molecular dipoles. This second process is responsible for the GER effect. It is informative to compare the salient features of these two types of polarization mechanisms and their implications on the ER effect.

An important common characteristic of ER fluids is the yield stress, i.e., the shear stress beyond which a solidified ER fluid breaks and starts to behave like a fluid. A non-Newtonian fluid that exhibits such behavior is generally denoted as a Bingham fluid in which the stress-shear rate relationship is given by $\tau = \tau_Y + \eta\dot{\gamma}$, where τ denotes the shear stress, τ_Y the yield stress, η the viscosity, and $\dot{\gamma}$ the shear rate. From dimensional analysis, τ_Y must be proportional to the (electric) polarization energy density $|\vec{P} \cdot \vec{E}|$, where $\vec{P} = N\vec{p}$ is the polarization density, with N the number density of the solid particles.

For induced polarization, $\vec{P} = \chi\vec{E}$, where $\chi = N\alpha$ is the dimensionless electric susceptibility. Hence $|\vec{P} \cdot \vec{E}| = \chi E^2$; i.e., yield stress varies quadratically with the electric field. Also, because there is a maximum value of polarizability $\alpha = R^3$, reached at the limit of $\epsilon_s/\epsilon_\ell \rightarrow \infty$, it follows that there is a maximum value for the dimensionless electric susceptibility $\chi = N\alpha \simeq R^3/(4\pi R^3/3) \sim 0.24$. This maximum value foreshadows the upper bound for the yield stress, $1.38\sqrt{R/\delta}(\epsilon_\ell E^2/8\pi)$, where δ denotes the separation between the particles. Because the applied electric field is always limited by the breakdown field, on the order of 5 kV mm^{-1} , the yield stress achievable by most of the traditional ER effect is usually on the order of a few kilopascals.

For molecular dipoles, the polarization is the result of competition between the alignment energy $-\vec{p}_0 \cdot \vec{E} = -p_0 E \cos \theta$ and thermal Brownian motion, where θ denotes the angle between the electric field and the molecular dipole moment p_0 . The thermally averaged dipole moment $\langle p \rangle$ is given by the Langevin function $\langle p \rangle = p_0(\coth x - x^{-1})$, where $x = p_0 E/k_B T$. For $x \ll 1$, we have $\langle \vec{p} \rangle = p_0 x/3 = [p_0^2/(3k_B T)]\vec{E}$, or $\alpha_p = p_0^2/3k_B T$. It follows that the electric susceptibility at room temperature has a value $\chi_p \sim N\alpha_p \approx 4\text{--}50$, depending on the (maximum) number density used. Regardless, $\chi_p \gg \chi$ by one to two orders of magnitude, which implies that there is the potential to break the yield stress upper bound imposed by the induced polarization mechanism, provided the molecular dipoles can be harnessed to an advantage. However, such expectation must be tempered by the fact that the electrical manifestations of molecular dipoles are usually masked either by random orientations, as in the liquid state, or by quadrupolar pairings, as in the case of solid configurations.

An important development in the study of ER fluids is the discovery of the GER effect in the dispersion of nanoparticles, comprising barium titanate oxalate $[\text{BaTiO}(\text{C}_2\text{O}_4)_2]$ coated with a nanoscale layer of urea molecules, in silicone oil (Wen et al. 2003). The GER fluid can exceed by one to two orders of magnitude the theoretical upper bound on the yield stress imposed by

Breakdown field: the value of the electric field at which an electrical breakdown would occur

the induced polarization mechanism, as well as exhibit a linear dependency of the yield stress on the electric field that is distinct from that in conventional DER fluids. Below we discuss the mechanism with which the molecular dipoles of the urea molecules, each with a dipole moment of 4.6 debyes, are harnessed in achieving the GER effect.

1.3. Outline of This Review

In what follows, Section 2 briefly reviews the DER mechanism and the conceptual advance that made its quantitative modeling possible. In particular, the variational effective dielectric constant formulation and the attendant implementation using Bergman-Milton representation theory are described, together with some comparisons with experiments. The GER effect and its theoretical underpinnings, both phenomenological and microscopic, are presented in Section 3. Section 4 addresses ER fluid dynamics from the continuum hydrodynamic point of view and presents results of a numerical implementation with predictions regarding the various aspects of Bingham fluid behavior. Section 5 briefly reviews the present status of the use of GER fluids to achieve digitally controlled functionalities in microfluidic chips.

2. MECHANISM OF THE DIELECTRIC ELECTORRHEOLOGICAL EFFECT

By using the model of induced dipole-dipole interactions, one can demonstrate that for a system of identical dielectric microspheres dispersed in insulating fluid, the lowest energy state is for the microspheres to aggregate and form columns along the applied field direction, with a microstructure inside the columns predictable from the dipole-dipole interaction (Tao & Sun 1991). However, such a simple picture leaves many questions unanswered. In particular, as the particles aggregate and touch, multipole interactions (those beyond the dipole interaction) necessarily become dominant, and the local field effect must also be taken into account. Conductivity and relaxational effects, appearing as the imaginary part of the particle or fluid dielectric constants, may also contribute to the DER effect. These complications make the theory of the DER effect quite complex, and hence most initial work in this area proceeded by direct simulations. Based on a theory incorporating the dynamics of both fluid and solid particles, Bonnecaze & Brady (1992a,b) performed simulations on systems comprising 25 or 49 particles, in two spatial dimensions. Klingenberg and colleagues (1989, 1991a,b, 1993; Klingenberg 1993) carried out simulations based on the interaction of point dipoles (subsequently also extended to beyond the point dipole limit) with hard core repulsion, coupled with Stokes hydrodynamic drag on the particles, aimed at understanding the rheology and kinetics of structure formation in DER fluids. Hass (1993) performed simulations excluding the Brownian force and analyzed the structure formation from his data. Similar studies were also performed by Tao's group (Tao & Jiang 1994, Gulley & Tao 1997). Wang et al. (1996, 2000) considered the many-body effect (e.g., as in the local field effect) and simulated structure formation and transition in ER fluids. Hu et al. (1994) conducted simulations by considering the torque on solid particles under an AC applied electric field and, based on a simple model, partly included two-body hydrodynamic interactions. Davis (1992a,b) carried out finite-element calculations to analyze the force arising from the polarization or conductivity of the particles. Conrad and coworkers (Chen et al. 1991, Chen & Conrad 1994, Conrad & Sprecher 1994, Shih et al. 1994, Tang et al. 1995a,b) have developed model theories, including the effects of the conductivity, along with experimental studies.

More recently, Yethiraj & van Blaaderen (2003) used confocal microscopy to experimentally explore the phase behavior of a colloidal system with a tunable interparticle interaction (from

hard sphere to soft) under an external electric field. Hynninen & Dijkstra (2005) calculated the Helmholtz free energy of similar systems using simulations and obtained a full phase diagram that agreed well with Yethiraj & van Blaaderen's experimental results. Bossis et al. (2007) developed a model that reproduced the experimentally measured size distribution of chains and their formation kinetics in DER fluids. Using confocal microscopy, Agarwal & Yethiraj (2009) found a novel cellular network phase in a low-density colloidal suspension on the application of a uniform AC field. Sun & Yu (2003) studied the ground state of DER fluids comprising particles with different dielectric constants, whereas Shen et al. (2006) investigated the microstructure of polydisperse DER fluids from an energetics point of view by using the finite-element method. Ivlev et al. (2008) reported the first observation of the DER effect in complex plasmas by performing a microgravity experiment as well as a molecular dynamics simulation. It should also be noted that Choi and coworkers (Cho et al. 2004, Choi & Jhon 2009) have devoted efforts to the fabrication of polymeric ER materials.

While much can be learned from simulations and experiments about the rheology and hydrodynamics of DER fluids, they nevertheless cannot lead to an overview of the DER mechanism that may allow, e.g., quantitative predictions on the DER rheological effect, resolution on the issue of the contribution from (or the lack of) the conductivity of the solid particles and the fluid, and the theoretical formulation for obtaining an upper bound on the DER effect. In particular, the upper bound can be useful in providing a picture of the characteristics of the optimal DER particles, as well as the necessary guidelines for engineering designs involving the use of DER fluids. The following section proposes a variational theory that can address all these relevant issues.

2.1. Variational Effective Dielectric Function Formulation

The microstructural variation accompanying the field-induced rheological characteristics should also have electrical manifestations. In particular, because the solid-fluid composite becomes anisotropic under the application of an electric field, such anisotropy must be reflected in the effective dielectric constant of the system. Here the effective dielectric constant is defined by

$$\langle \vec{D} \rangle = \tilde{\epsilon}_{eff} \langle \vec{E} \rangle, \quad (2a)$$

$$\tilde{\epsilon}_{eff} = \begin{pmatrix} \bar{\epsilon}_{xx} & \bar{\epsilon}_{xy} & \bar{\epsilon}_{xz} \\ \bar{\epsilon}_{yx} & \bar{\epsilon}_{yy} & \bar{\epsilon}_{yz} \\ \bar{\epsilon}_{zx} & \bar{\epsilon}_{zy} & \bar{\epsilon}_{zz} \end{pmatrix}, \quad (2b)$$

where $\langle \vec{D} \rangle$ denotes the spatially averaged displacement field, $\langle \vec{E} \rangle$ is the spatially averaged electric field (assumed to be along the z direction), and the matrix elements of $\tilde{\epsilon}_{eff}$ are complex in general [in the form of $\kappa + i(4\pi\sigma/\omega)$, with σ the conductivity and ω the angular frequency of the applied electric field].

The concept of the effective dielectric constant is based on the nature of the electromagnetic wave interaction with inhomogeneous materials. When the wavelength is much larger than the scale of the heterogeneities, the microstructure can no longer be resolved, and the composite appears homogeneous to the probing wave. In that limit, the electromagnetic response of the composite is fully captured by the effective dielectric constant tensor (Bergman & Stroud 1992).

The effective dielectric constant–tensor elements are dependent on the relative volume fraction(s) of the constituents and their respective dielectric constants, as well as the anisotropy and the microstructure of their arrangement. In particular, differences in the close-packed microstructures ought to be reflected in the effective dielectric constant–tensor elements, provided the theory for their evaluations is sufficiently accurate.

The dielectric constant tensor directly participates in the Gibbs free energy density expression f of the fluid-solid composite:

$$f = -\frac{1}{8\pi} \vec{E} \cdot \text{Re}(\bar{\epsilon}_{eff}) \cdot \vec{E} - TS = -\frac{1}{8\pi} \text{Re}(\bar{\epsilon}_{zz}) E^2 - TS, \quad (3)$$

where S denotes entropy, and $\text{Re}(\)$ means that we take the real part of the quantity in the parenthesis. As the stated focus of this review is the ER effect, we may treat the entropy term as small when compared to the electrical part of the energy. A variational formulation of the DER problem may then be obtained by requiring the minimization of f through the maximization of $\text{Re}(\bar{\epsilon}_{zz})$ with respect to the microstructure of the solid particles (Ma et al. 1996). A successful program in carrying out this maximization would not only obtain the DER ground-state structure, but also lay the basis for the quantitative evaluation of the rheological characteristics that can arise from the distortion of such a structure (Ma et al. 1996, Tam et al. 1997).

The variational effective dielectric constant approach solves, in one step, all the difficulties posed above. In particular, the local field effect and the multipole interactions are all accounted for, provided the effective dielectric constant can be evaluated accurately. In addition, the contribution of the imaginary part of the dielectric constant may also be incorporated through the imaginary parts of the components' dielectric constants.

2.2. Effective Dielectric Constant: The Bergman-Milton Spectral Representation

To evaluate $\bar{\epsilon}_{zz}$, we find that the Bergman-Milton spectral function representation (Bergman 1978a,b, 1985; Milton 1979, 1981a,b, 2002; Bergman & Stroud 1992) of the effective dielectric constant provides the best approach for our purposes. The starting point of our considerations is the Laplace equation

$$\nabla \cdot [\epsilon(\vec{r}) \nabla \varphi(\vec{r})] = 0. \quad (4)$$

Here φ is the electrical potential, i.e., $\vec{E} = -\nabla \varphi$, and $\epsilon(\vec{r})$ is the local dielectric constant, given by

$$\epsilon(\vec{r}) = \epsilon_\ell \left[1 - \frac{1}{s} \vartheta(\vec{r}) \right], \quad (5a)$$

where

$$s = \frac{\epsilon_\ell}{\epsilon_\ell - \epsilon_s}, \quad (5b)$$

ϵ_ℓ denotes the liquid dielectric constant, and ϵ_s is the solid dielectric constant. Here ϑ is the characteristic function, defined to be 1 inside the solid particles and zero elsewhere. The microgeometric information of the system is captured by ϑ . In contrast, the parameter s (which can be complex) contains the material characteristics. For later developments, it is important to note that if the dielectric constants are real, then the value of s is either greater than 1 or less than zero. In other words, a real s cannot take any value between zero and 1. Equation 4 is to be solved with the boundary conditions $\varphi(x, y, z = 0) = 0$ and $\varphi(x, y, z = L) = L$ (i.e., average $E_z = -1$). As $\bar{\epsilon}_{zz}$ is defined by

$$\bar{\epsilon}_{zz} = \frac{1}{V} \int dV \{ \epsilon_\ell [1 - \vartheta(\vec{r})] + \epsilon_s \vartheta(\vec{r}) \} \frac{\partial \varphi(\vec{r})}{\partial z}, \quad (6)$$

it is not difficult to show that (see below) it can be expressed in the spectral representation

$$\bar{\epsilon}_{zz} = \epsilon_\ell \left(1 - \frac{1}{V} \sum_u \frac{|\langle z | \varphi_u \rangle|^2}{s - s_u} \right), \quad (7)$$

where φ_u and s_u are respectively the eigenfunctions and their associated eigenvalues of the integral (Hermitian) operator $\hat{\Gamma}$, defined as

$$\hat{\Gamma} = \int dV' \vartheta(\vec{r}') \nabla' G(\vec{r}, \vec{r}') \cdot \nabla'. \quad (8)$$

Here $G(\vec{r}, \vec{r}') = 1/4\pi |\vec{r} - \vec{r}'|$ is the Green function, and $\hat{\Gamma}$ is Hermitian with the following definition of the inner product:

$$\langle \psi | \varphi \rangle = \int dV \vartheta(\vec{r}) \nabla \psi^*(\vec{r}) \cdot \nabla \varphi(\vec{r}). \quad (9)$$

Equation 7 can be derived by first noting that Equation 6 can be expressed in the inner product form as

$$\bar{\varepsilon}_{zz} = \varepsilon_\ell \left(1 - \frac{s^{-1}}{V} \langle z | \varphi \rangle \right).$$

A formal solution of the potential may be obtained by rewriting Equation 4 as a Poisson equation:

$$\nabla^2 \varphi = \frac{1}{s} \nabla \cdot [\vartheta(\vec{r}) \nabla \varphi].$$

Solving this equation by integrating the inhomogeneous source term on the right-hand side with the Green function yields

$$\varphi = z + \frac{1}{s} \hat{\Gamma} \varphi,$$

where z represents the homogeneous part of the solution, given by the applied electric field $E_z = -1$. A formal solution of the potential is then obtained as

$$\varphi = \left(1 - \frac{1}{s} \hat{\Gamma} \right)^{-1} z.$$

This formal solution can be expanded in terms of the $\hat{\Gamma}$ operator's eigenfunctions as

$$|\varphi\rangle = \sum_u \left(1 - \frac{1}{s} \hat{\Gamma} \right)^{-1} |\varphi_u\rangle \langle \varphi_u | z \rangle = \sum_u |\varphi_u\rangle \frac{s}{s - s_u} \langle \varphi_u | z \rangle.$$

Substitution of this formal solution into the inner product form of $\bar{\varepsilon}_{zz}$ leads to Equation 7.

The integral operator $\hat{\Gamma}$ is noted to be a projection operator, as can be seen from Equation 8, because the Green function may be regarded as the inverse of the Laplacian operator (two successive gradient operators). Hence the eigenvalues of $\hat{\Gamma}$ lie between zero and 1.

In Equation 7, V is the sample volume, a normalization factor. The most remarkable feature of this equation, which is exact, is that the material properties, given by s , are completely separated from the geometric information (contained in φ_u and s_u) as filtered by the Laplacian. Because both the solid and liquid dielectric constants can be complex, s is a complex number in general. At the same time, it is clear that if s is real, then its value as given by Equation 5b should be either less than zero or greater than 1, as noted above. Because both $|\langle z | \varphi_u \rangle|^2$ and s_u are real, with the additional constraint that $0 < s_u < 1$ as already stated, it follows that $s - s_u$ can approach zero only in limiting cases, i.e., at zero and 1, and these cases define the upper bounds for the shear modulus and yield stress, described below. Equation 7 also makes clear that the imaginary

Table 1 Comparison of the effective $\bar{\epsilon}_{zz}$ for various lattice structures

ϵ_s/ϵ_ℓ		Structure					
		BCT	FCC	HCP	BCC	SC	Diamond
10	Exact	2.167	2.156	2.156	2.043	1.911	1.627
	Dipole	2.031	1.994	1.995	1.905	1.734	1.601
800	Exact	5.173	5.129	5.129	4.205	3.518	1.976
	Dipole	3.376	3.188	3.194	2.798	2.230	1.897

Abbreviations: BCT, body centered tetragonal; FCC, face centered cubic; HCP, hexagonal closed packed; BCC, body centered cubic; SC, simple cubic.

parts of the dielectric constants can indeed contribute to $\text{Re}(\bar{\epsilon}_{zz})$ (through the complex material parameter s) and hence the DER effect.

2.3. Predictions of the Variational Formulation and Comparisons with Experiments

By using the spectral representation and the effective dielectric constant formulation, quantitative predictions become possible for a DER fluid comprising uniform-sized microspheres dispersed in an insulating liquid.

2.3.1. Ground-state microstructure. For uniform-sized microspheres, the lowest energy state should correspond with a periodic microstructure that maximizes $\text{Re}(\bar{\epsilon}_{zz})$. The computational formalism for the numerical evaluation of Equation 7 has been detailed elsewhere (Ma et al. 2003, Sheng & Wen 2010). The calculated values of $\bar{\epsilon}_{zz}$ for the various structures are shown in **Table 1**, at two ratios of $\epsilon_s/\epsilon_\ell = 10$ and 800. In the calculations, the separation between the spheres is 5×10^{-3} in units of R , and the volume fraction of solid particles is 0.2. For comparison, results using just the dipole approximation are also shown. In **Table 1**, for the effective dielectric constant values inside the close-packed columns, the face centered cubic value is in fact slightly larger than that for the body centered tetragonal (BCT) value, owing to the higher packing density. However, when averaged over the whole sample, the BCT value always wins slightly, regardless of the values of the material constants or solid volume fractions.

Experimentally, Wen et al. (1999) multiply coated microspheres with a glassy core diameter of $34 \pm 2 \mu\text{m}$ with a 2- μm layer of Ni, a 1.5- μm layer of lead zirconate titanate (PZT), another 1- μm layer of Ni, and finally a 1- μm layer of TiO_2 . The overall diameter of the microspheres is thus $45 \pm 2 \mu\text{m}$. The ground-state microstructure under an electric field of 2 kV mm^{-1} was studied by dispersing the microspheres in epoxy. After solidifying the epoxy matrix, the authors cut the sample along the (001) and (110) planes and visualized it with scanning electron micrographs (**Figure 2**). The square lattice in **Figure 2a**, along the (001) plane, and the tight packing lattice in **Figure 2b**, along the (110) plane, uniquely determine the crystal structure to be BCT, thus verifying the theoretical prediction. Another approach, using laser diffraction, was adopted by Chen et al. (1992) to verify the ground-state structure. The same result, the BCT structure, was obtained.

2.3.2. Shear modulus and yield stress. The rheological characteristics can be calculated by first defining the relevant distortion. For the shear modulus and yield stress, the distortion is shown in the inset of **Figure 3**, in which θ , the angle of distortion relative to the external E field, is the

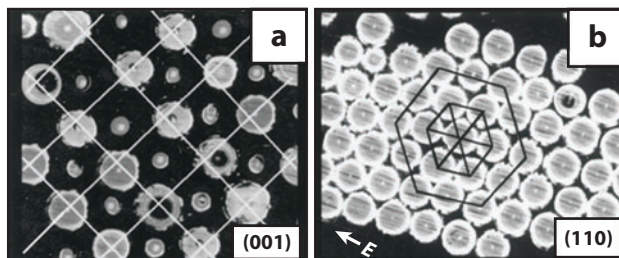


Figure 2

Body centered tetragonal structure formed by multiply coated microspheres under an electric field (2 kV mm^{-1}). The structure is frozen in epoxy and visualized through cross-sectional scanning electron micrographs. In panel *a*, the cut was along the (001) plane, and in panel *b*, the cut was along the (110) plane. Figure adapted from Wen et al. (1999).

strain variable. For the BCT lattice, shearing in the direction perpendicular to the z axis creates not only a tilt away from the electric-field direction by an angle θ , but also a distortion in the lattice constants c and a given by $c/R = 2/\cos\theta$, $a/R = [8 - (c^2/2R^2)]^{1/2}$. Thus under shear, the volume fraction of solid spheres in the BCT structure is also dependent on θ . For small θ , $\bar{\varepsilon}_{zz}(\theta)$ may be expanded about its optimal value as

$$\text{Re} \left[\frac{\bar{\varepsilon}_{zz}(\theta)}{\varepsilon_\ell} \right] = \text{Re} \left[\frac{\bar{\varepsilon}_{zz}(0)}{\varepsilon_\ell} \right] - \frac{1}{2} \mu \theta^2 + \dots, \quad (10)$$

where μ denotes the shear modulus (Ma et al. 1996). Again by using the spectral representation approach to calculate the electrical energy, we show a numerically evaluated stress versus strain curve in **Figure 3**. By definition, the stress is given by $dE(\theta)/d\theta$. At small strain, the slope of the linear variation is the shear modulus. The peak of the stress-strain curve corresponds to the yield stress beyond which the system becomes unstable. Experimental consistency with theory prediction may be obtained together with the optimal particle structure, shown below.

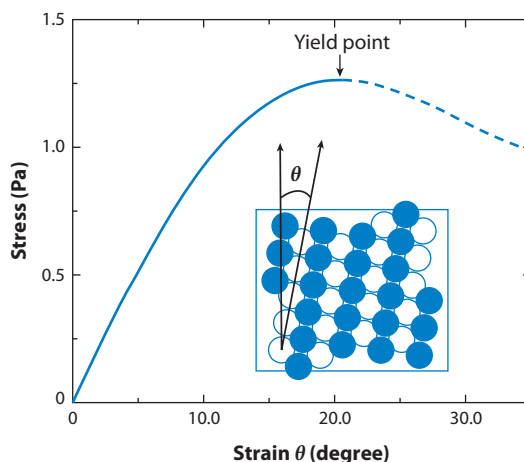


Figure 3

Calculated stress plotted as a function of strain, i.e., the tilt angle θ as defined in the inset. The dashed line indicates the unstable regime. The maximum stress is defined as the static yield stress. Here the curve is calculated with $\varepsilon_1 = 2.7$, $\varepsilon_s = 8.4 + 0.43i$, the volume fraction of the spheres is 22%, and the applied field is 1.3 kV mm^{-1} . Figure adapted from Ma et al. (1996).

2.3.3. Upper bounds and optimal particle structure. The upper bounds (Ma et al. 2003) to the shear modulus and yield stress are directly related to the potential for the divergence of $\bar{\varepsilon}_{zz}$ shown in the spectral representation. From Equation 7, this can only happen when the denominator on the right-hand side vanishes, i.e., when both s and s_u approach either zero or 1. Here we present the case of the zero limit. To obtain the physical upper bounds, we let $\varepsilon_s \rightarrow \infty$ so that $s \rightarrow 0$. We also note that s_u would approach zero only when the spheres touch. Hence a (small) separation δ between the surfaces of the neighboring spheres is specified, and the shear modulus and yield stress are evaluated as a function of the ratio δ/R . The upper bounds thus obtained are $1.9(R/\delta)$ for the shear modulus and $1.38\sqrt{R/\delta}$ for the static yield stress, both in units of the energy density $\varepsilon_\ell E^2/8\pi$. For $\delta = 1 \text{ \AA}$ (atomic separation) and $R = 20 \text{ }\mu\text{m}$, we get $15,120(\varepsilon_\ell E^2)$ for the maximum shear modulus and $617(\varepsilon_\ell E^2)$ for the maximum yield stress. If $\varepsilon_\ell = 2.5$ and $E = 1 \text{ kV mm}^{-1}$, these expressions translate into 4 MPa and 8 kPa, respectively.

To verify the particle size R and separation δ dependencies of the yield stress upper bound, researchers fabricated doubly coated microspheres with uniform-sized glassy cores and Ni and TiO_2 outer coatings, using the electroless plating (for the Ni coating) and sol-gel (for the TiO_2 coating) methods sequentially. Two different sizes of the core glass microspheres were used (1.5 μm and 50 μm in diameter). Here the Ni coating makes the microspheres polarizable enough so that we can take s to be nearly zero, and the TiO_2 coating sets a value for δ .

Figure 4 compares the measured yield stress values with those calculated from the effective dielectric constant formulation (Tam et al. 1997). The increased size of the particles clearly increases the yield stress, in approximately the square-root ratio as predicted by the upper-bound expression. In addition, the absolute values of the measured yield stress are well accounted for by the calculations using approximate values of the TiO_2 -coating thicknesses. For comparison, we have also measured and calculated the yield stresses for pure glass spheres, and those with just TiO_2 coatings. Both are orders of magnitude smaller. The calculated value for pure TiO_2 spheres of similar size is also much smaller. The simple physical picture that emerges from these results is that (a) the DER yield stress is closely related to the electrostatic energy of the system, and (b) for

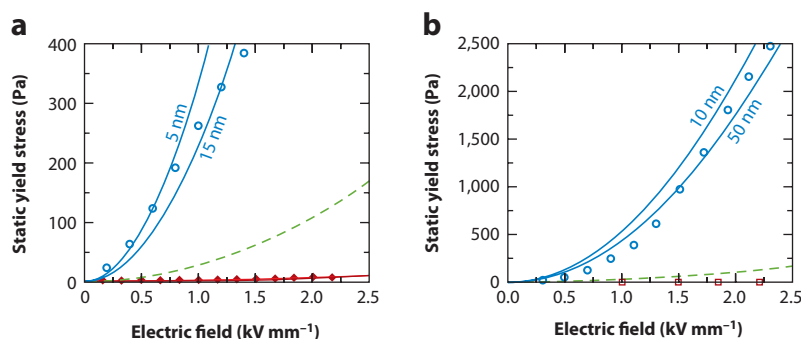


Figure 4

The measured (blue symbols) and calculated (blue lines) static yield stresses of an electrorheological fluid using (a) 1.5- μm doubly coated particles and (b) 50- μm doubly coated particles. From the vertical scales, it is seen that the larger particles exhibit a larger yield stress in roughly the square root of the size ratio. For comparison, the figure also shows the calculated yield stress for solid TiO_2 particles of the same size (green dashed lines), the measured yield stress for pure glass spheres (barely seen as the open red squares on the horizontal axis of panel b) of the same size, and the measured yield stress for glass spheres coated just with TiO_2 (filled red diamonds on the horizontal axis shown in panel a), without Ni, of the same size. Figure adapted from Tam et al. (1997).

a given applied electric field, the electrostatic energy can be maximized by the field distribution and dielectric constant of the materials. The metallic coating of the doubly coated microspheres limits the field distribution to the dielectric areas occupied by the TiO_2 coating and the silicone oil. The thin TiO_2 coatings ensure small separations, thus producing high internal fields. The enhanced ER effect is the result (Tam et al. 1997).

The doubly coated glassy microspheres are in a sense ideal for the DER effect. However, the requirement of large sphere size is not optimal from an application point of view because large microspheres also tend to sediment, unless the density can be matched with that of the fluid.

LCR meter:

meter that measures electrical inductance, capacitance, and resistance

2.3.4. Anisotropy and nonlinearity of the effective dielectric constant. As the variational approach is based on the optimization of the effective dielectric constant, it is important to check experimentally if the dielectric constant indeed increases and displays anisotropy under the application of an electric field. However, when the applied field is fairly large, it is difficult to determine the dielectric constant along the electric-field direction. To overcome this difficulty, investigators have utilized the similarity in the microstructure under an electric field with that under a magnetic field.

Special particles were prepared as silica spheres $35 \pm 3 \mu\text{m}$ in diameter coated with an inner Ni layer and an outer dielectric layer, such as PZT and TiO_2 , formed by using electroless plating and sol-gel processes, respectively. These particles respond to both the electric field and the magnetic field. The dielectric constants along the z (magnetic-field direction) and x directions ($\bar{\epsilon}_{zz}$ and $\bar{\epsilon}_{xx}$), measured by an LCR meter, are shown in **Figure 5** (Ma et al. 2003). Whereas $\bar{\epsilon}_{zz}$ displays an increasing trend with the magnetic field, as expected, the $\bar{\epsilon}_{xx}$ component displays a slight decrease. These trends are independent of whether the outer coating is PZT or TiO_2 . The theory predictions of the asymptotic dielectric constant values, obtained by using the spectral function approach, are shown in **Table 2**. Here the inputs to the calculations are determined by

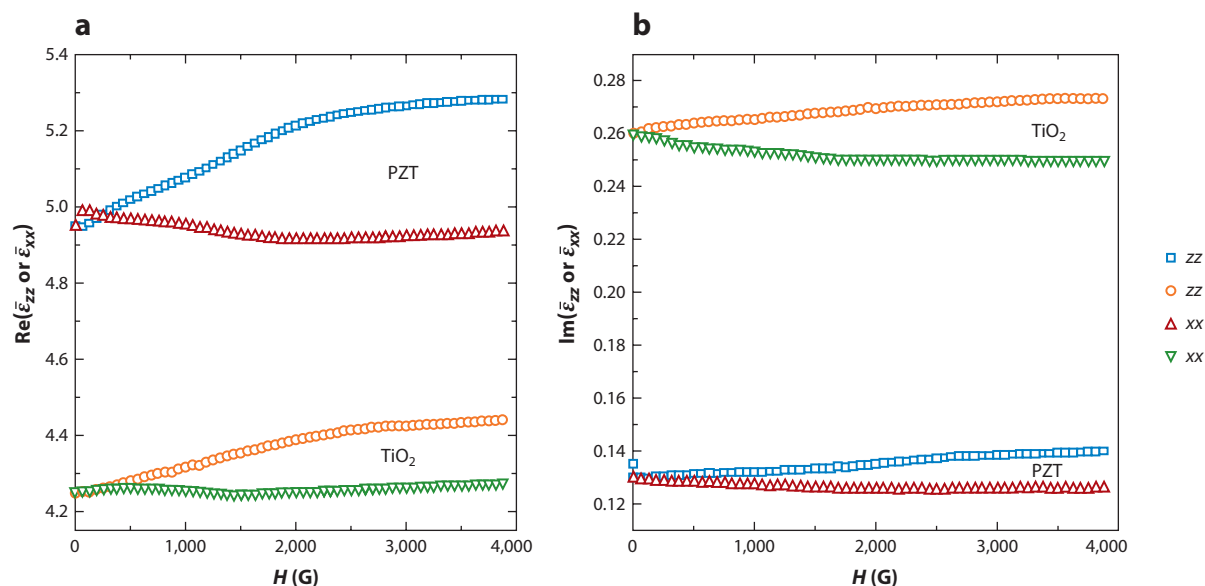


Figure 5

Dependences of the (a) real (Re) and (b) imaginary (Im) parts of the dielectric constant on the applied magnetic-field strength. Here the volume fraction is 0.27, and the frequency of the LCR meter is fixed at 1 kHz. Figure adapted from Ma et al. (2003).

Table 2 Theory-experiment comparison for the zz and xx components of the effective dielectric constants

Structure		Theory		Experiment	
		$\text{Re}(\bar{\epsilon})$	$\text{Im}(\bar{\epsilon})$	$\text{Re}(\bar{\epsilon})$	$\text{Im}(\bar{\epsilon})$
Random		Fitted	Fitted	4.95	0.13
PZT coating	zz	5.67	0.23	5.29	0.14
	xx	4.75	0.11	4.94	0.12
Random		Fitted	Fitted	4.26	0.26
TiO_2 coating	zz	4.56	0.37	4.44	0.28
	xx	4.15	0.23	4.25	0.25

the values of the real and imaginary parts of the effective dielectric constants when the system is isotropic ($H = 0$). It is seen that reasonably good agreement is obtained.

3. MECHANISM OF THE GIANT ELECTORRHEOLOGICAL EFFECT

Since its discovery (Wen et al. 2003), the GER mechanism has been a topic of interest. Huang et al. (2006) have presented a phenomenological model. Tan et al. (2009) calculated local electric fields between two particles using the finite-element approach and concluded that the local field can cause a saturation polarization of the coated polar molecules. Shen et al. (2009) proposed a model based on the interaction between polar molecules and the induced charge on the particles to explain the alignment of molecular dipoles. In terms of materials fabrication, Cheng et al. (2009, 2010), Lu et al. (2009), Shen et al. (2009), Yin & Zhao (2004), and Wang et al. (2007) have synthesized different types of inorganic materials that exhibit the GER effect. Below we base the exposition of the GER effect on the material system of urea-coated nanoparticles of barium titanate oxalate (Wen et al. 2003).

3.1. Characteristics of Giant Electrorheological Fluids

Figure 6a shows the structure of GER particles, comprising a ~ 50 -nm core of barium titanate oxalate, with a 5-nm coating of urea (Wen et al. 2003). **Figure 6b** shows the column formation

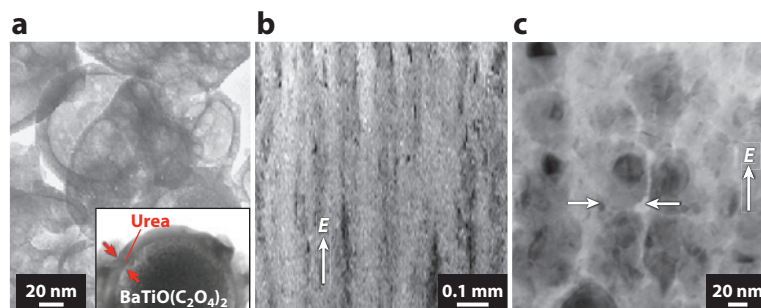


Figure 6

Images of nanoparticles in giant electrorheological suspensions. (a) Transmission electron micrograph of coated nanoparticles. The urea coatings, ~ 5 nm in thickness, are clearly seen. (b) Optical microscope image of a sample prepared in epoxy, solidified under an applied field E of 2 kV mm^{-1} . Columns aligned along the field direction are visible. (c) Transmission electron micrograph of a section of the column shown in panel b. The arrows indicate one of the flattened interfaces. Figure adapted from Wen et al. (2003).

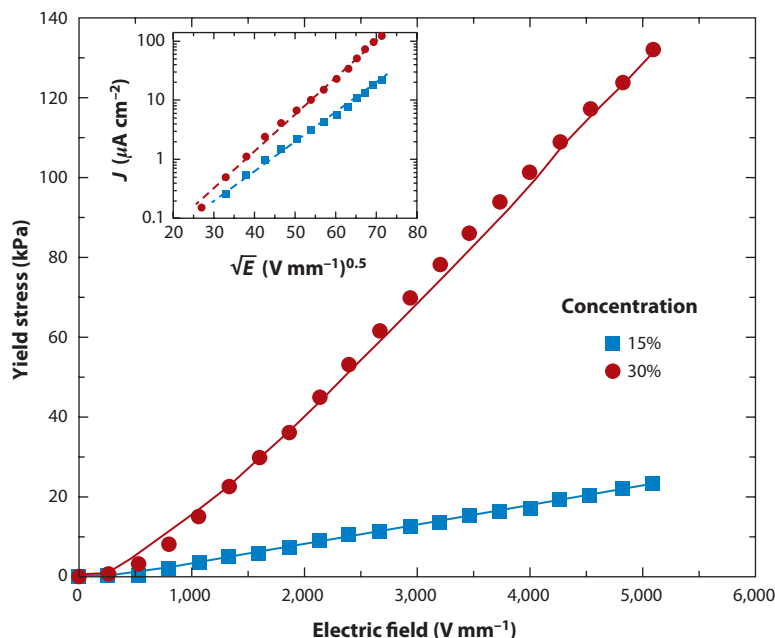


Figure 7

Static yield stress plotted as a function of the applied electric field for two solid concentrations. The symbols denote experiment, and the solid lines are theory. (*Inset*) Logarithm of the current density J plotted as a function of \sqrt{E} . The dashed straight lines serve to delineate the relationship $\ln J \sim \sqrt{E}$, indicating the mechanism of activation over the Coulomb barrier (the Poole-Frenkel effect). At the very moderate field of 1 kV mm⁻¹, the linear behavior of the yield stress is already established, indicating that a saturated polarization layer contributes to the giant electrorheological effect. Figure adapted from Wen et al. (2003).

when an electric field was applied. **Figure 6c** illustrates that under an electric field, the coatings of the nanoparticles are significantly deformed, indicating a degree of softness in the coating.

Figure 7 plots the measured yield stress and current density (shown in the inset) as a function of the applied electric field. A prominent feature is the near-linear dependency of the yield stress on the electric field. This is only possible if the yield stress arises not from induced polarization, but rather from the saturation polarization of permanent molecular dipoles so that in the expression $-\vec{P}_o \cdot \vec{E}$, the polarization density is a constant, and the resulting yield stress is therefore linear in the applied field, with a magnitude that can break the theoretical upper bound for the induced polarization mechanism.

It should be noted that GER fluids are very oil sensitive. By using silicone oil, one can obtain the effect shown in **Figure 7**, but with the same particles dispersed in pure decane, the GER effect can disappear completely (Gong et al. 2008). Such a large contrast implies that oil plays a synergistic role in the GER effect. An important clue to this oil sensitivity is the consistency of the mixture one can obtain by using two different oils, e.g., silicone oil and decane. For silicone oil, the consistency is like that of light yogurt, but for decane the consistency is like that of mud. Therefore, the particles can be better dispersed in silicone oil than in decane; i.e., there is a wetting effect between silicone oil and GER particles.

Another qualitative difference between GER and DER fluids lies in the yield stress scaling with respect to the particle size. For DER fluids, we demonstrate above that the yield stress varies roughly as \sqrt{R} ; i.e., larger particles imply a larger ER effect. However, in GER fluids, the yield

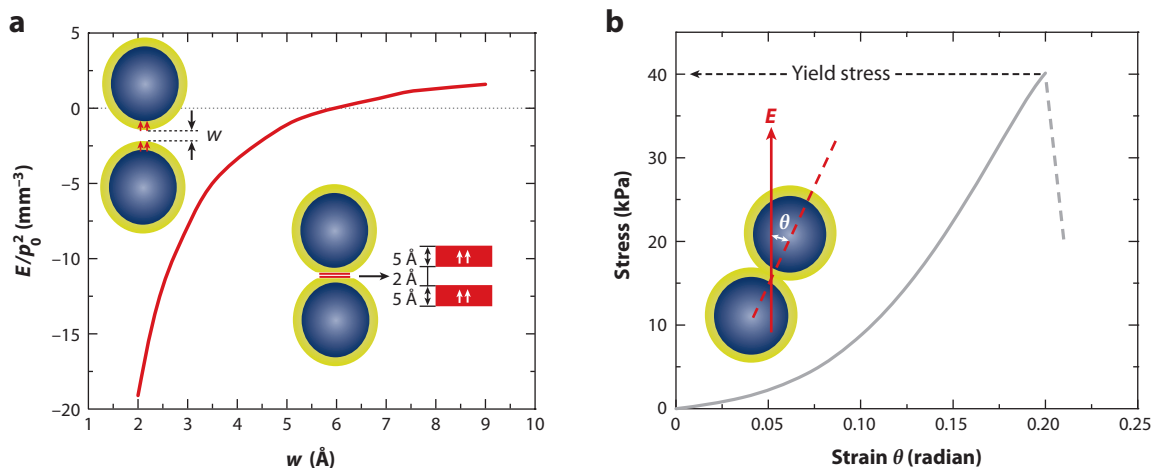


Figure 8

Illustration of the phenomenological model of the giant electrorheological effect with calculated results. (a) Shown in the upper left is a schematic picture of our model, consisting of two coated spheres, each with a 50-nm-diameter core and a 5-nm coating (both with $\epsilon = 60$). The gap, with width w , has $\epsilon = 2$ (for silicone oil). The solid curve shows the calculated interaction energy divided by p_0^2 between two pairs of nearest-neighbor surface dipoles, each with $p_0 = 4.6$ debyes and separated laterally by 4.5 Å ($\epsilon = 1$ between the dipoles), when w increases from 2 Å . (b) The stress numerically calculated from the finite-element method, at an electric field of 2 kV mm^{-1} , is plotted as a function of the strain. The yield stress point corresponds to the point of separation between the two spheres. Figure adapted from Wen et al. (2003).

stress varies as $1/R$ (Wen et al. 2004), implying that the GER effect is interfacial in character so that smaller particles would display a larger effect.

3.2. A Phenomenological Model of the Giant Electrorheological Effect

A phenomenological model was formulated to explain the GER effect (Huang et al. 2006). It is based on the following elements.

The foremost assumption of the phenomenological model is that the molecular dipoles of urea can form aligned dipolar layers in the contact region between two coated nanoparticles, under a moderate applied electric field. This is the source of the strong adhesion responsible for the GER effect and is shown schematically in **Figure 8a**. At distances larger than 10 nm , i.e., in the noncontact state, the application of an electric field will induce some orientational polarization (as described by the Langevin function) in the molecular dipoles, and the approach to contact will follow the DER mechanism described above.

The equilibrium contact state is represented by the balance of the (attractive) electrostatic force with the (repulsive) elastic force, with the elastic deformation of the two coated spheres in contact given by the Hertzian solution (Huang et al. 2006). Mathematical details of the model are presented in **Supplemental Appendix A** (follow the **Supplemental Material** link from the Annual Reviews home page at <http://www.annualreviews.org>).

The predictions of the model are in good agreement with measured results, as seen in **Figure 7**. In particular, the linear dependency on the applied electric field and the magnitude of the GER effect is a direct reflection of the surface saturation polarization. Another prediction of the model is that because the effect owes its origin to interfacial saturation polarization, more surface area (hence smaller particles) would enhance the GER effect. This turns out to be the case (Wen et al. 2004).

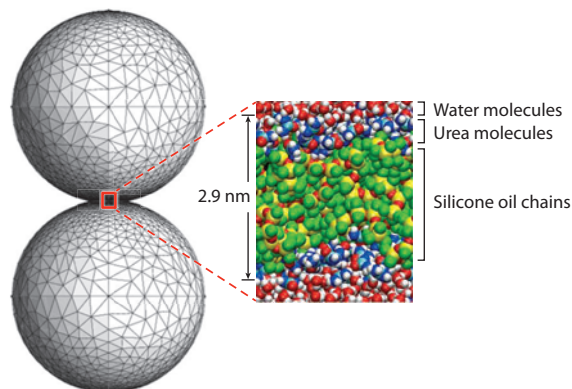


Figure 9

Molecular model of the contact area between two spherical nanoparticles. Here green, red, and yellow in the middle of the right panel denote the silicone oil chains. The urea molecules (with *dark blue* denoting nitrogen) are located on the two sides of the silicone oil film, and the water molecules are located on the top and bottom sides.

However, the phenomenological model does not address the issues related to the energetics inside the aligned dipolar layer and the observed synergism with silicone oil. Below we give a microscopic understanding of how the saturation polarization arises in the contact region of two solid particles.

3.3. Microscopic Mechanism of the Giant Electrorheological Effect

We used the molecular dynamics code GROMACS (Alejandre et al. 1995, Sides et al. 2002, Mountain & Thirumalai 2004, Lee & van der Vegt 2006, van der Vegt et al. 2006), which can account for molecular interactions at the atomic/molecular level by using empirically derived parameter values, to simulate a urea–silicone oil mixture trapped in a nanocontact between two polarizable particles. This is shown schematically in **Figure 9**.

Figure 10a shows what happens when a 0.2-V nm^{-1} electric field is applied across the gap (Chen et al. 2010). Three urea molecular filaments are clearly seen snaking through the porous

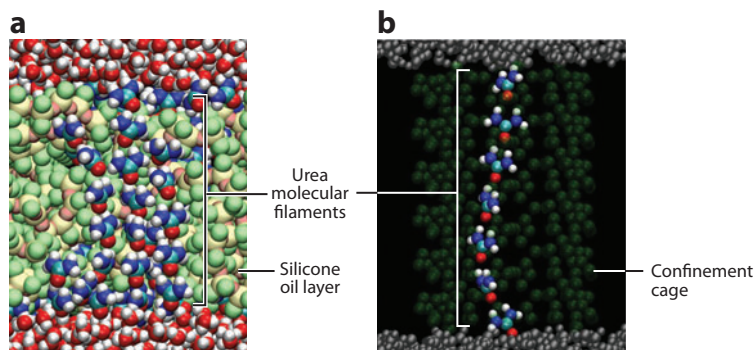


Figure 10

(a) Urea molecular filaments across a silicone oil layer under a 0.2-V nm^{-1} electric field and (b) in an $\sim 1\text{-nm}$ cylindrical confinement cage under a 0.1-V nm^{-1} electric field. Figure adapted from Chen et al. (2010).

oil chains to bridge the two surfaces. Inside each filament, the dipoles are predominantly aligned. In contrast, we have also conducted a simulation in which the gap region is occupied completely by the liquid-like urea molecules (but with the same bounding surfaces with the water molecules). We found that at least 0.6 V nm^{-1} of electric field is required to partially align the urea molecules; i.e., there is a lowering of the required electric field for dipole alignment by a factor of two to three. The two simulation cases considered, with and without the silicone oil chains, are meant to correspond to the wetting and nonwetting cases, respectively, because only if the silicone oil wets the particles would it be situated inside a nanoscale gap; otherwise a nonwetting oil would be excluded, and a gap full of urea molecules is a more likely scenario.

To confirm that the confinement effect of the silicone oil chains is playing a major role, we have artificially constructed a cylindrical confinement cage by using positionally fixed Lennard-Jones particles with the same force-field parameters as the methyl group, and the result obtained at 0.1 V nm^{-1} is shown in **Figure 10b**, in which a filament of aligned molecular dipoles is clearly seen. As the cage does not undergo thermal Brownian motion, the cage's confinement effect is shown to be much more effective, evidenced by the formation of a filament at a field nearly one order of magnitude smaller than that required for liquid-state urea.

A simple explanation of this phenomenon is that the one-dimensional (1D) confinement decreases the orientational entropic phase space of the urea dipoles and thereby significantly increases the urea dipoles' sensitivity to the applied field (Chen et al. 2010). This effect may be mathematically formulated: Whereas for the 3D case we have $\langle p \rangle_{3D}/p_0 = \coth(p_0 E/k_B T) - (k_B T/p_0 E)$, where $p_0 = 4.6$ debyes for urea molecules, in the 1D case, it is given by $\langle p \rangle_{1D}/p_0 = \tanh(p_0 E/k_B T)$. At any given E , $\Delta p = \langle p \rangle_{1D} - \langle p \rangle_{3D}$ is always positive (e.g., at 0.3 V nm^{-1} the difference is 2.12 debyes); therefore, $-\Delta p \cdot E$ provides a driving energy/force for the urea molecules to develop a more diffuse interface with the oil film, in the form of 1D filaments penetrating the oil film (under an electric field), which is porous on the molecular scale. This is especially the case as the number of hydrogen bonds per urea molecules is nearly the same in either the 3D amorphous state or the 1D filaments. Also, in the limit in which $p_0 E/k_B T \ll 1$, it is easy to see that in one dimension, $\alpha_m = p_0^2/k_B T$, which is exactly a factor of three larger than that in three dimensions.

It should be noted that there are hydrogen-bonding interactions in the system. But the number of hydrogen bonds in the 1D filament configuration is well balanced against that in the 3D dispersion; hence the 3D-to-1D crossover in the urea molecules' microgeometry emerges as the dominant factor. Moreover, as $E \rightarrow \infty$, we have $\Delta p \rightarrow k_B T/E$, which implies that $-\Delta p \cdot E$ approaches a constant value, $-k_B T$, independent of E . This is consistent with the simulation results showing that as $E \rightarrow \infty$, there is a saturation behavior for the maximum gap width ($\sim 9 \text{ nm}$) beyond which no filament formation was observed. This behavior is consistent with the surface scaling aspect of the GER effect (Wen et al. 2004, Chen et al. 2010). $\Delta p \cdot E \rightarrow k_B T$ is noted to arise from the difference of two degrees of freedom between the 3D and 1D case; hence two times $(1/2)k_B T$ (the equipartition energy) is exactly $k_B T$.

GROMACS simulations also confirm the synergism with silicone oil (Gong et al. 2008) because it is polar (having oxygen atoms in its chains) and thus more permeable to urea. It also wets the urea-coated nanoparticles.

The formation of aligned dipolar filaments provides a ready explanation for the observed yield stress versus electric-field behavior, as the yield stress is directly proportional to the electrical energy density. This can be seen as follows. For a linear stress-strain (τ - ε) relationship $\tau = a\varepsilon$, the yield stress is given by $\tau_Y = a\varepsilon_o$, with ε_o the critical strain. Because the energy density is given by $(1/2)a\varepsilon^2$, we thus have $\tau_Y = 2W_o/\varepsilon_o$, where $W_o = (1/2)a\varepsilon_o^2$. That is, the yield stress is proportional to the energy density as deduced above from dimensional analysis. If the stress-strain

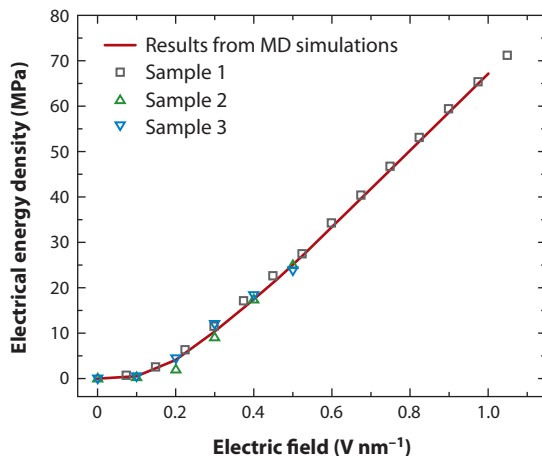


Figure 11

Electrical energy density plotted as a function of the electric field in the nanogap (*red curve*). Scaled data from three sets of experiments are superposed on the curve. The electric field E is obtained from the measured field E_m by $E = \alpha E_m$, where α is the field enhancement factor. The measured yield stress Y is related to the electrical energy density ΔW by $\Delta W = \beta Y / 10$, where β is the volume dilution factor. The values of (α, β) for sample 1 (Wen et al. 2003), sample 2 (Wen et al. 2004), and sample 3 (Gong et al. 2008) are (281.2, 7,590), (100, 974), and (100, 1,010), respectively. Figure adapted from Chen et al. (2010).

relationship is not strictly linear, the constant a can be adjusted to account for its effect on the energy density.

We have calculated the total potential energy density of the simulation box at different fields, with the zero-field total potential energy density subtracted off. The resulting difference ΔW is negative, indicating a large attraction between the two bounding surfaces. Plotted in **Figure 11** is the variation of $|\Delta W|$ as a function of the electric field. To compare with experimental data, one must scale this energy density by a volume dilution factor β for the energy density of the GER fluid because the nanoscale gap considered here constitutes the region of closest approach between two nanoparticles. Hence the gap electrical energy should be averaged over a volume on the order of d^3 , with d the nanoparticle diameter. For $d \sim 50$ – 100 nm and our sample volume of 190 nm^3 , $\beta \sim 1,000$ – $10,000$. Also, as noted above, the field in the contact region is enhanced by a factor $\gamma \sim 100$ – 300 when compared with the externally applied field. All three data sets shown in **Figure 11** agree well with the curve obtained from the MD simulations, and the values of α and β fall within the physically reasonable range.

4. ELECTORRHEOLOGICAL FLUID DYNAMICS

It is desirable to have a continuum hydrodynamic theory for ER fluids because discrete particle simulations, even at the level of point dipole interactions only, simply cannot routinely handle the large systems that are necessary for comparison with experiments. The Onsager variational principle offers a systematic approach to derive the equations of motion by accounting for two important elements in our complex system: dissipation and free energy. A description of the Onsager principle, together with the derivation of the ER hydrodynamic equations of motion and their numerical implementation, is given in **Supplemental Appendix B**. Here we present the model, the relevant continuum hydrodynamic equations of motion, and simulation results (Zhang et al. 2008a). For simplicity, we consider only DER fluids in the limit of dipole interactions.

[▶ Supplemental Material](#)

4.1. Two-Phase Model of Dielectric Electrorheological Fluids

Under an electric field, the DER fluid phase separates into a dense phase, comprising a fluid-solid mixture in which the particles are arranged in either chains or columns with some structure inside (denoted as the s phase) and a liquid phase (denoted as the ℓ phase). This is clearly seen in **Figure 1**. Accordingly, for the s phase we treat the solid particles, consisting of identical microspheres with radius R , collectively by regarding their density $n(\vec{x}) = f_s(\vec{x})(4\pi R^3/3)^{-1}$ as a field variable, where $f_s(\vec{x})$ denotes the dimensionless, local volume fraction of solid microspheres. One can write down the total energy for the s component under an externally applied electric field \vec{E}_{ext} , including the interaction between the particles and between the particles and the external field, as a functional of $n(\vec{x})$:

$$F[n(\vec{x})] = \frac{1}{2} \int G_{ij}(\vec{x}, \vec{y}) p_i(\vec{x}) n(\vec{x}) p_j(\vec{y}) n(\vec{y}) d\vec{x} d\vec{y} - \int \vec{E}_{ext}(\vec{x}) \cdot \vec{p}(\vec{x}) n(\vec{x}) d\vec{x} + \frac{\varepsilon_0}{2} \int \left(\frac{R}{|\vec{x} - \vec{y}|} \right)^{12} n(\vec{x}) n(\vec{y}) d\vec{x} d\vec{y}, \quad (11)$$

where $G_{ij}(\vec{x}, \vec{y}) = \vec{\nabla}_i \vec{\nabla}_j |\vec{x} - \vec{y}|^{-1}$ is the dipole interaction operator, and $\varepsilon_0(R/|\vec{x} - \vec{y}|)^{12}$ is the repulsive interaction between the particles (Klingenberg 1991a) introduced to avoid singularities in the calculations, with ε_0 a suitable energy scale. In Equation 11, the Einstein summation convention is followed, in which the repeated indices imply summation. A variation of F with respect to n leads to $\delta F = \int \mu(\vec{x}) \delta n d\vec{x}$, where

$$\mu[n(\vec{x})] = -\vec{E}_{ext}(\vec{x}) \cdot \vec{p}(\vec{x}) + \int G_{ij}(\vec{x}, \vec{y}) p_i(\vec{x}) p_j(\vec{y}) n(\vec{y}) d\vec{y} + \varepsilon_0 \int \left(\frac{R}{|\vec{x} - \vec{y}|} \right)^{12} n(\vec{y}) d\vec{y} \quad (12a)$$

is the chemical potential for the s component. The first two terms on the right-hand side of Equation 12a may be interpreted as the product of the local electric field \vec{E}_l with the (induced) dipole moment, $-\vec{E}_l \cdot \vec{p}$, where

$$[\vec{E}_l(\vec{x})]_i = [\vec{E}_{ext}(\vec{x})]_i - \int G_{ij}(\vec{x}, \vec{y}) p_j(\vec{y}) n(\vec{y}) d\vec{y}. \quad (12b)$$

From the local electric field, the induced dipole moment $\vec{p}(\vec{x})$ is obtained from Equation 1 in which the CM factor β is replaced by $f_s(\vec{x})\beta$. This is because in the CM factor ε_s should be replaced by the effective dielectric constant $\bar{\varepsilon}_s(\vec{x})$ within the s phase, and from the Maxwell-Garnett equation we have

$$\frac{\bar{\varepsilon}_s(\vec{x}) - \varepsilon_\ell}{\bar{\varepsilon}_s(\vec{x}) + 2\varepsilon_\ell} = f_s(\vec{x})\beta. \quad (13)$$

The equations of motion (for their derivation, see **Supplemental Appendix B**) are given by

$$\frac{\partial n}{\partial t} + V_s \cdot \nabla n = \frac{1}{\gamma} \nabla \cdot n \nabla \mu, \quad (14)$$


$$\rho_s \left(\frac{\partial \vec{V}_s}{\partial t} + \vec{V}_s \cdot \nabla \vec{V}_s \right) = -\nabla p_s + \nabla \cdot \tau_{visc}^s + n \nabla \mu + K(\vec{V}_\ell - \vec{V}_s), \quad (15)$$

$$\rho_\ell \left(\frac{\partial \vec{V}_\ell}{\partial t} + \vec{V}_\ell \cdot \nabla \vec{V}_\ell \right) = -\nabla p_\ell + \nabla \cdot \tau_{visc}^\ell + K(\vec{V}_s - \vec{V}_\ell), \quad (16)$$

where V_s and V_ℓ are the s phase and ℓ phase velocities, respectively; $p_{s,\ell}$ is the s (ℓ) phase pressure; $\tau_{visc}^{s,\ell} = \eta_{s,\ell}(\nabla \vec{V}_{s,\ell} + \nabla^T \vec{V}_{s,\ell})/2$ is the viscous stress tensor in the respective phase, with $\eta_{s,\ell}$ denoting its viscosity; and $\rho_\ell, \rho_s = nm + (1 - f_s)\rho_\ell$ are the mass densities, with m the mass of the solid particle. We note that η_s is implicitly a function of f_s with a dependency shown in **Supplemental Figure 1**, and $K = 9f_s\eta_\ell/2R^2$ and $\gamma = 6\pi\eta_s R$ are the two constants. The equations of motion

are supplemented by the subsidiary (incompressibility) conditions $\nabla \cdot \vec{V}_{s,\ell} = 0$, together with the boundary conditions of normal components of $\nabla\mu$, with $\vec{V}_{s,\ell}$ zero at the solid boundary, and no tangential slip for $\vec{V}_{s,\ell}$.

Equation 14 is in the form of a continuity equation for the number density n . The right-hand side is the divergence of a current density derived from the Onsager principle. In accordance with the linear response framework, this current density is proportional to the gradient of a potential—the chemical potential in the present case. Because in the linear response framework the current density and the force density are linearly related, here by the coefficient γ , we find that the force density $n\nabla\mu$ also appears on the right-hand side of Equation 15. Through the chemical potential, this term contains all the electrical effects, such as the dipole-dipole interaction. The last terms on the right-hand sides of Equations 15 and 16 represent the relative friction between the two phases; hence they have opposite signs. The first two terms on the right-hand sides of Equations 15 and 16 are standard in the Navier-Stokes equation. However, the viscosity for the s phase, whose behavior is given in **Supplemental Figure 1**, is noted to be the Newtonian component of the colloidal viscosity, applicable only at low shearing rates. At moderate to high shearing rates, the effective viscosity can be lower than that indicated in **Supplemental Figure 1**, but that will not materially affect the predicted behaviors shown below.

 **Supplemental Material**

4.2. Predictions and Experimental Verification

We present theory predictions on two Bingham fluid characteristics: the yield stress, which can have either a static or a dynamic value, and the Poiseuille flow profile. Another type of prediction is on the electrode configuration dependency of the shear stress, which is beyond the Bingham fluid model.

4.2.1. Bingham fluid characteristics. A Bingham fluid is defined by its yield stress beyond which a DER fluid behaves as a Newtonian fluid (with a linear dependency of the shear stress versus shear rate). Experimentally, one can always obtain two yield stress values—the static and the dynamic—and they are usually different. To theoretically calculate the static yield stress, we put a layer of DER fluid between two parallel plates and moved the top plate relative to the bottom plate, as shown in the inset of **Figure 12a**. The curve connecting the data points shows the calculated result for an applied field of 2 kV mm^{-1} . The stress and strain relation displays a maximum beyond which the stress decreases with increasing strain, implying instability. Hence the maximum point is the static yield stress, 374 Pa. For the results shown in **Figure 12b**, the top plate moves at a constant speed relative to the bottom plate, and the calculated shear stress displays fluctuations as a function of time (inset of **Figure 12b**) that is commonly observed experimentally, a consequence of the breaking and reconnecting of the columns. The figure displays the averaged value as a function of shear rate. Extrapolation to zero shear rate yields the dynamic yield stress, 278 Pa, much smaller than the static value under the same applied field, which is usually the case.

In another comparison with a Bingham fluid, we show the Poiseuille flow profile between two parallel plates. In **Figure 13**, the velocity profile is that of a DER fluid with the same parameter values as those shown in **Figure 12**, under an electric field of 4 kV mm^{-1} . The similarity with a Bingham fluid is clearly seen, although there exists some quantitative difference.

4.2.2. Electrode configuration dependency of the shear stress–shear rate relationship.

Under flow, the shear stress–shear rate relationship for an ER fluid can be sensitive to the manner

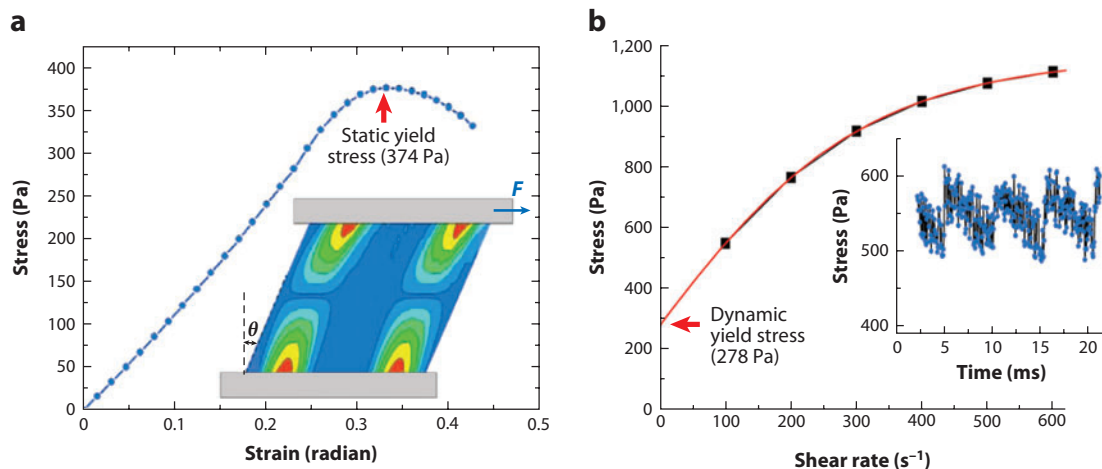


Figure 12

(a) Calculated shear stress plotted as a function of strain (the angle θ) under an electric field of 2 kV mm^{-1} . The cell is $650 \mu\text{m}$ by $650 \mu\text{m}$ by $2R$ (y direction), with a periodic boundary condition along the shearing direction x . To facilitate the formation of columns under an electric field, the initial density is given by $n_0 + \delta n \cdot \cos(kx)$. The red arrow denotes the static yield stress (374 Pa). (Inset) The breaking of the columns around the yield stress point. Here red indicates a high value of n and blue a low value. (b) Calculated (averaged) dynamic shear stress under the Couette flow condition for the same cell as in panel a. By extrapolating to zero shear rate, the dynamic yield stress is found to be 278 Pa. (Inset) The stress fluctuations at a shear rate of 100 s^{-1} . Here $R = 5 \mu\text{m}$, $m = 1.2 \times 10^{-9} \text{ g}$, $\epsilon_s = 10$, $\epsilon_1 = 2$, $\eta_1 = 10 \text{ cP}$, $\rho_1 = 0.96 \text{ g cc}^{-1}$, and overall $f_s = 30\%$. Figure adapted from Zhang et al. (2008a).

under which the electric field is applied. Such an effect is beyond the Bingham fluid description of ER fluids. We compare our results directly with experiments.

The conventional manner is to apply an electric field perpendicular to the flow direction. This is shown in the inset of **Figure 14**, which plots the pressure drop across a Poiseuille flow, representative of the averaged shear stress, against the averaged shear rate, which can be

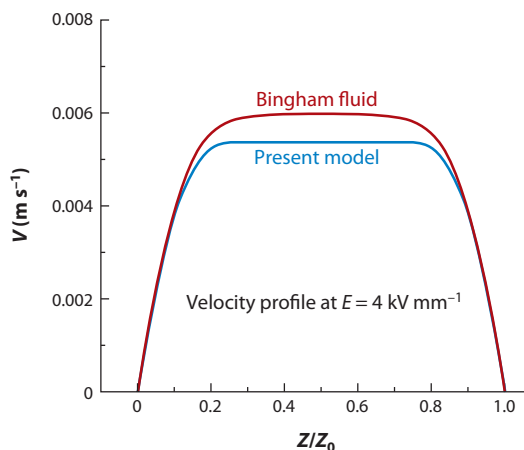


Figure 13

Poiseuille flow profile between two parallel planes denoted $z/z_0 = 0, 1$ ($z_0 = 650 \mu\text{m}$). The simulation parameter values are the same as those shown in **Figure 12**. The yield stress and viscosity values for the Bingham fluid are the dynamic yield stress evaluated from the present model and the colloidal viscosity at 30% solid particle concentration (see **Supplemental Figure 1**).

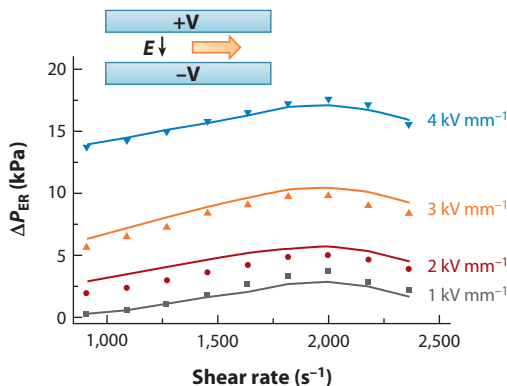


Figure 14

The (time-averaged) pressure difference due to the electrorheological (ER) effect, plotted as a function of shear rate for the electrode configuration (with a gap of 1 mm) shown in the inset. The solid lines are the continuum calculations from our theoretical results, and the symbols represent data from a Poiseuille flow experiment. The applied electric field is 1 (*gray*), 2 (*red*), 3 (*orange*), and 4 (*blue*) kV mm^{-1} . At 1 kV mm^{-1} , the pressure difference is very small at low shear rates. Here, $R = 2.5 \text{ }\mu\text{m}$, $m = 1.2 \times 10^{-12} \text{ g}$, $\epsilon_s = 2.9$, $\epsilon_f = 2$, $\eta_f = 50 \text{ cP}$, $\rho_f = 0.96 \text{ g cm}^{-3}$, and overall $f_s = 11.5\%$. Figure adapted from Zhang et al. (2008a).

evaluated from the volume flow rate with the relevant simulated flow profile (such as that seen in **Figure 13**). There is a maximum beyond which the apparent viscosity of the ER fluid decreases; i.e., there is a shear-thinning effect.

Heuristically, it is easy to understand this shear-thinning effect because the strength of the columns is always along the applied electric field. Hence, when the columns are tilted significantly away from the perpendicular field direction, the resistance to shear is decreased.

Figure 15 shows an alternative electrode configuration in which one uses comb-type interdigitated fingers lying in the bounding planes (illustrated in the inset). In this configuration, there is a significant component of the electric field that lies parallel to the flow direction. Indeed, both theory and experiment show no shear-thinning effect as in the conventional electrode configuration.

5. GIANT ELECTORRHEOLOGICAL FLUID-BASED MICROFLUIDICS

The field of microfluidics deals with the behavior, precise control, and manipulation of fluids that are geometrically restricted to small, typically submillimeter scales. Since the field's origin approximately two decades ago, many studies and investigations have been conducted (Manz et al. 1990). Its impact spans across engineering, physics, chemistry, microtechnology, and biotechnology. There are generally two types of microfluidic approaches: continuous flow and droplet flow. The latter is more challenging owing to its complex operations. The special utility of droplet-based microfluidic systems lies in the formation of uniform droplets and therefore, intrinsic to such systems, and of utmost importance, the precise control of the droplets' size, shape, and monodispersity. There are many different approaches to microdroplet generation, such as integrated flow-focusing geometry onto a microfluidic device. This microfluidic flow-focusing method is often used in droplet/bubble formation (Jensen & Lee 2004, Garstecki et al. 2005), whereas another geometry-based generation method uses a T junction, by which two immiscible fluids are brought together. For droplet manipulation, many methods have been reported to date, such as geometry-based pressure control for droplet mixing (Liau et al. 2005), merging (Liu et al. 2007, Tan et al. 2007), and sorting (Link et al. 2006, Tan et al. 2008). Many active control methods have

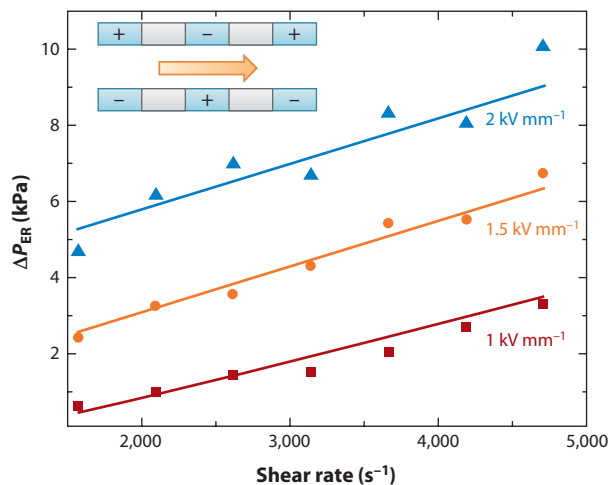


Figure 15

The pressure difference due to the electrorheological (ER) effect plotted as a function of shear rate for the planar, alternate electrode configuration. The symbols and lines represent the experimental and our theoretical results, respectively. The electric field is equal to 1 (*red*), 1.5 (*orange*), and 2 (*blue*) kV mm^{-1} . Here, $R = 2.5 \mu\text{m}$, $m = 1.2 \times 10^{-12} \text{ g}$, $\epsilon_s = 2.9$, $\epsilon_f = 2$, $\eta_f = 50 \text{ cP}$, $\rho_f = 0.96 \text{ g cm}^{-3}$, and overall $f_s = 11.5\%$. Figure adapted from Zhang et al. (2008a).

also been realized recently, such as hydrostatic pressure (Luo et al. 2007), temperature gradient (Mazouchi & Homsy 2001), thermal expansion (Zhu et al. 2005), optical approaches (Baroud et al. 2007, Jeffries et al. 2007), magnetic field (Psaltis et al. 2006), and electrical control (Joung et al. 2000, Ahn et al. 2006, Priest et al. 2006, Chabert & Viovy 2008), including electrostatic (Link et al. 2006), electrokinetic effect (Indeikina & Chang 2002), dielectrophoresis (Schwartz et al. 2004), and electrowetting (Pollack et al. 2002, Ren et al. 2003, Paik et al. 2003).

Recent experiments have shown that GER fluids can be used as highly effective smart mediums to develop different types of microfluidic components, owing to their strong ER response. Below we present droplet manipulation and microfluidic logic gates based on the use of GER fluid droplets. Successful implementations of GER fluid-based valves, pumps, and microfluidic mixers are presented in **Supplemental Appendix C**.

5.1. Microfluidic Droplet Manipulation

Droplet microfluidics has attracted increasing attention from diverse fields because it requires only a small amount of materials and less time, produces less waste, and has the potential of highly integrated and computer-controlled reaction processes for chemistry and biology. In previous work, we employed a microfluidic flow-focusing approach together with a digital control system to generate GER droplets with which some applications have been realized (Zhang et al. 2008b, 2009; Niu et al. 2007, 2009). In the following, we review some recent results of GER fluid-based microfluidic droplet generation and manipulation as well as the pertinent achievements.

GER droplets can be generated by a flow-focusing approach shown in **Figure 16a**, in which a continuous-phase GER fluid (nanoparticles mixed with sunflower oil) and two streams of pure silicone oil were injected into the main channel through a center inlet and two side inlets, respectively. By properly controlling the flow rates of both the GER fluid and silicone oil, one can

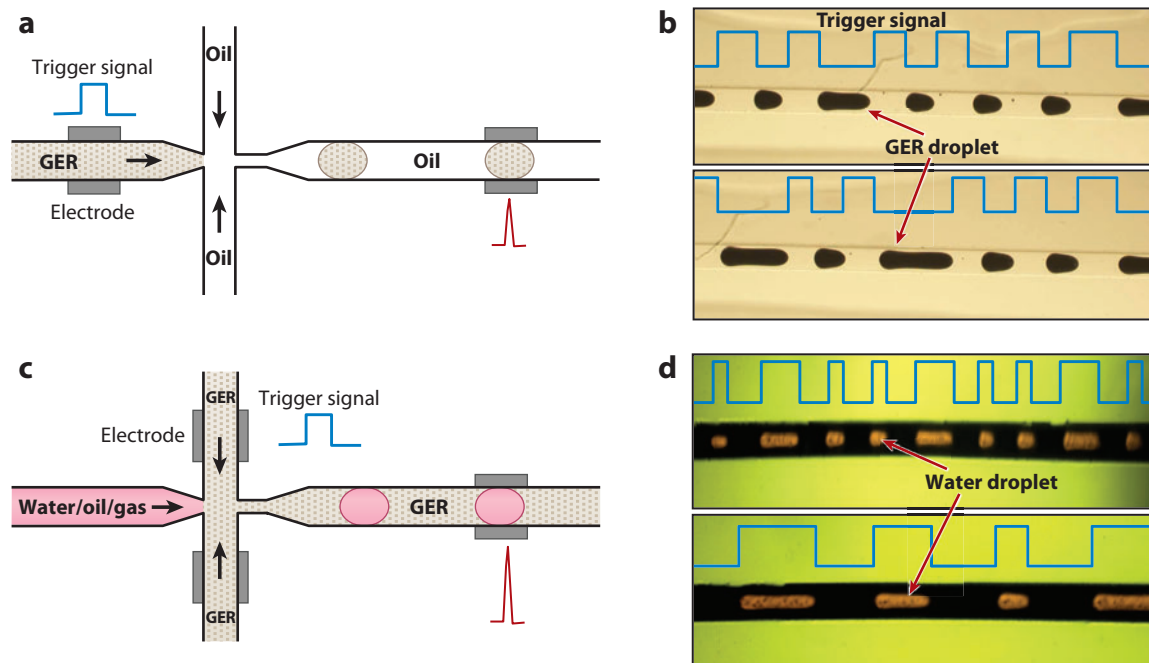


Figure 16

(a,c) Schematic view of giant electrorheological (GER)- and water-droplet generation with the flow-focusing approach. (b,d) Optical images of the generated (b) GER and (d) water droplets. Figure taken from Niu et al. (2009).

generate GER droplets in a passive manner. However, when an electric field (with a trigger signal $\sim 2 \text{ kV mm}^{-1}$) is applied to the upstream electrode, the flow behavior of the GER fluid changes from fluid to solid-like, and the GER fluid flow can be fully stopped, leaving only silicone oil being injected into the main channel. When the electric field is lower than a critical value, the GER flow resumes. Thus the flow of the GER droplets can be tuned actively through the signal modes. **Figure 16b** shows that there can be a clear correlation between the length of the electrical pulse and the length of the droplets. With the same device, water or gas bubbles can be generated digitally by the ER fluid (**Figure 16c**). Whereas the water/gas is injected into the main channel directly, the GER fluid is injected through the two side channels. The optical images, for the case of water, can be seen in **Figure 16d** (Niu et al. 2007).

To manipulate the status of the GER droplet in the microfluidic channel, one must have the detection and feedback capabilities. We use two parallel electrodes on the side channel walls to function as a capacitor that is connected to an external inductance. An LCR resonator is formed as shown in **Figure 17a**. Owing to the dielectric contrast between the carrier fluid (oil) and the GER droplet, the resonance frequency can be chosen such that when a GER droplet fills in the space between the electrodes, the detected signal amplitude is the highest (**Figure 17b**). Minimum signal output occurs when the space between the electrodes is filled with oil. For a GER fluid, water and the carrier fluid (oil) have different dielectric constants, so the relevant capacitances and resonances reflecting different droplet compositions can give rise to significantly different signal amplitudes (Zhang et al. 2009). Such detection is in situ and in real time, as well as sensitive, accurate, and fast ($> 1100 \text{ Hz}$). It requires no special sample preparation.

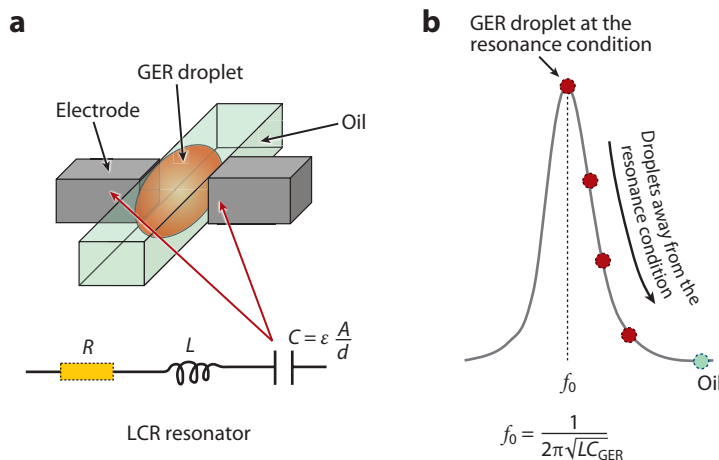


Figure 17

Schematics of giant electrorheological (GER) droplet detection via the capacitance approach. The output detected signal is shown schematically in panel *b*. Figure adapted from Niu et al (2007).

A GER fluid, together with a detection circuit, is useful in achieving accurate droplet control. Although GER fluid droplets can themselves be manipulated through the applied electric field (Zhang et al. 2008b), they can also be used to deliver a package containing a certain number of other passive droplets to the targeted destination. One such example, shown in **Figure 18**, demonstrates how water droplets can be delivered in varying amounts to the desired location on a chip, required in many chemical reactions and bioprocessings. By injecting GER droplets among the water-droplet trains, one can form packages of any desired number of water droplets sandwiched between two GER droplets. **Figure 18b,c** shows the schematics for one part of such a chip and some snapshots of the experimental results. By controlling the GER droplets, which can be digitally programmed, one can direct, sort, and deliver the train of water droplets to targeted destinations at which mixing, heating, or other processing may be carried out.

5.2. Giant Electrorheological Fluid–Based Microfluidic Logic Gate

Electronic devices have evolved from the vacuum tube—the first electronic logic gate. The logic function of this near-legendary component has been successfully mimicked by fluidic diodes, microelectrochemical logic (Zhan & Crook 2003). In the microfluidic domain, researchers have scrutinized both kinetic fluid regulation (Groisman et al. 2003, Rhee & Burns 2009) and static geographical stream manipulation (Cheow et al. 2007, Prakash & Gershenfeld 2007, Mosadegh et al. 2010, Weaver et al. 2010) as possible fluidic analogs. Simple logic devices such as the AND/OR gate, the static fluid transistor, and the oscillator are among the list of the achievements. They are limited, however, in that they either entail bulky peripheral equipment for round-trip manipulation or have complicated 3D microstructures.

The basic schematics of a GER fluid logic-gate design are illustrated in **Figure 19**, in which two parallel channels separated by a conducting gap are used to pass the GER fluid and the signal fluid. Two electrodes, *a* and *b*, are formed on the walls of two respective channels, while another conducting gap *c* that interconnects both the GER fluid channel and the signal fluid channel serves as another electrode. Because the carrier fluid is an oil with very low conductivity, the application

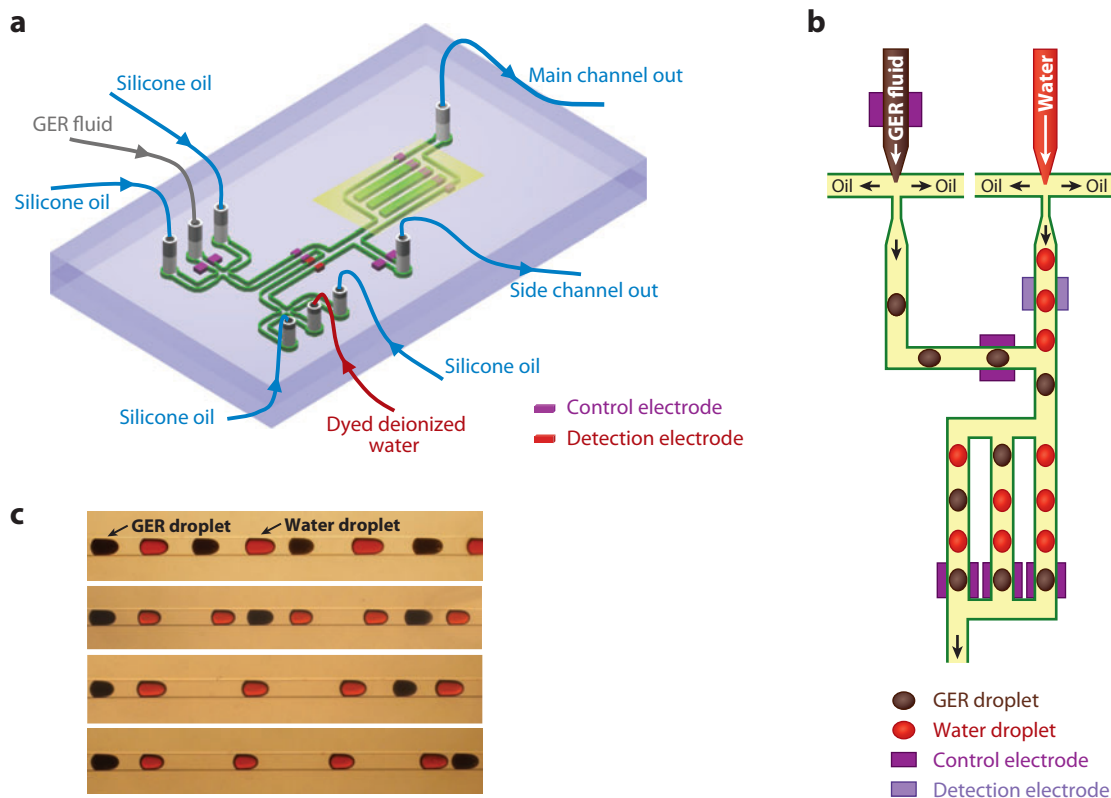


Figure 18

(a) A microchip generating giant electrorheological (GER) and water microfluidic droplets. (b) Schematic of the detection and sorting of GER and water droplets. (c) A map and optical microscopic images of GER droplets controlling the water droplets. Figure adapted from Zhang et al. (2009).

of high voltage across electrodes a and b has no effect on the conducting gap c. However, when a signal droplet moves into the regions denoted as electrodes b and c, a positive potential will be transmitted to the conducting gap through the signal droplet (as it is usually more conducting than the carrier oil), and thus the high voltage would be applied to the GER fluid, thereby solidifying it. That is, the variable gap voltage leads to a voltage differential V_G across the GER channel. V_G could be either off, wherein the voltage is not above the threshold required to completely solidify GER, or on, causing the GER fluid to solidify and stop flowing in the GER channel. From this design, the GER flow status thus can be tuned by the signal droplet.

The above basic design can be easily expanded into the OR and AND gate designs. When the fundamental structure is repeated in series like those shown in **Figure 20a**, the GER flow depends independently on the presence of droplets in channels 1 and 2. Thus a solidification in either one will stop the overall flow of the GER fluid, making this structure an OR gate. An AND gate design is presented in **Figure 20b**, in which voltage is shared evenly across the three channels, and only if water droplets are present in both control channels simultaneously would the GER flow be stopped. Because the GER flow is solidified only when both channels contain a droplet, the structure is a logical AND gate.

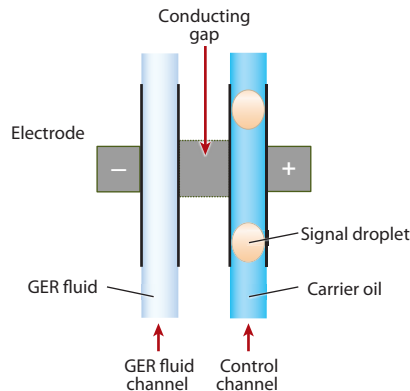


Figure 19

The fundamental logic-gate operation with a giant electrorheological (GER) fluid.

A microfluidic inverter (Wang et al. 2010) is illustrated in **Figure 21a**. To achieve this NOT function, signal electrodes and output electrodes (electrodes on the GER fluid channel) are joined in series, while the input voltage is applied across electrodes 1 and 2. In this case, the signal fluid is a high-conductivity solution, which can be modeled as a conductor, and the carrier fluid is an insulating oil. When the carrier oil flows between the signal electrodes, the circuit can be viewed as open, and the GER fluid continues its flow (output = 1). When the signal droplet is present between the signal electrodes, the circuit closes and a voltage is thus applied onto the output electrodes to stop the GER fluid flow (output = 0). **Figure 21b,c** presents the images for the ON and OFF operations' outputs, respectively. In this manner, the generated GER droplets are complementary to the signal droplets; hence a NOT operation, or a phase inversion, is achieved. With the same design but different operation coding arrangement, the universal logic gate has been achieved.

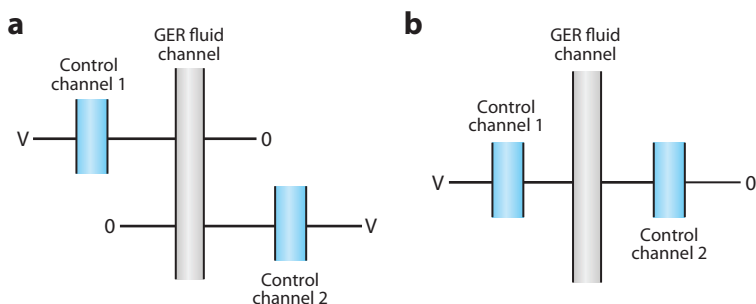


Figure 20

(a) An OR gate created by placing two giant electrorheological (GER) switches in series. For the GER fluid to stop flowing, either channel 1 or channel 2 must be filled with a droplet. (b) A simplified structure of an AND gate created by the mirroring of a single logic gate across the GER channel.

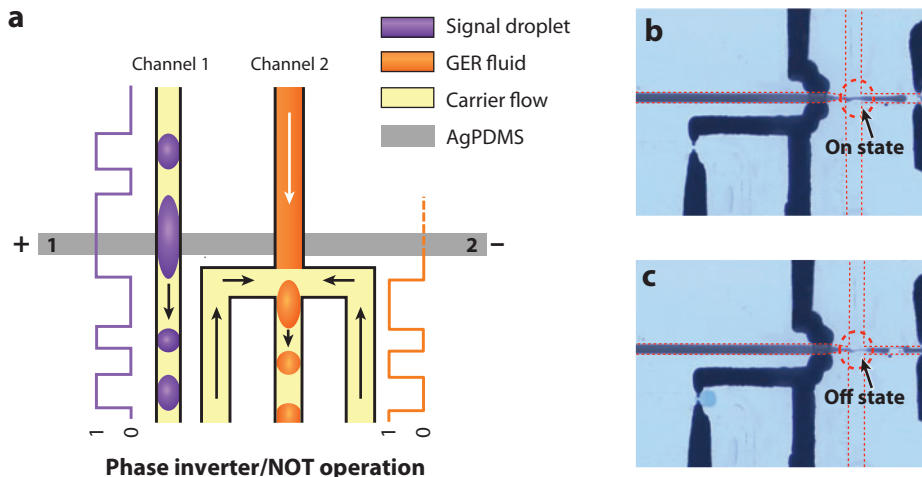


Figure 21

(a) Basic working principle of the logic gate, illustrated by a microfluidic inverter. The presence of the signal droplet between the signal electrodes will solidify the giant electrorheological (GER) fluid, while the presence of the carrier oil releases the GER fluid. (b) When the carrier oil flows between signal electrodes, the GER fluid flows continuously in the flow-focusing configuration. (c) When a signal droplet passes through the signal electrodes, the GER fluid is solidified. In this manner, the GER fluid is stopped so only the carrier oil flows. That is, the GER fluid is cut into droplets with phases complementary to that of the signal droplet. Hence this represents a phase inverter, or a NOT operation. Figure adapted from Wang et al. (2010).

SUMMARY POINTS

1. The DER effect is based on induced dipoles arising from the dielectric constant contrast between the solid particles and the fluid. DER fluids' ground-state structure, shear modulus, yield stress, and its upper bound can be obtained variationally from the effective dielectric constant formulation, by using the Bergman-Milton spectral representation for $\bar{\epsilon}_{zz}$.
2. The GER effect is based on the formation of molecular dipole filaments bridging the surfaces of two solid nanoparticles when they come into contact. It exhibits an orders-of-magnitude-larger ER effect as well as qualitatively different behaviors than those of DER fluids.
3. A continuum formulation of DER fluid dynamics can be obtained by using the Onsager variational principle. It is based on a two-phase description of DER fluids.
4. Theoretical predictions regarding the DER's ground-state structure, yield stress, and dielectric constant nonlinearity have found good experimental support.
5. The application of GER fluids to microfluidic chips has enabled the design and implementation of digitally controlled GER pumps, actuators, and individual droplet sensing and routing. In particular, through the use of GER fluid droplets, the microfluidic logic gates have been realized.

FUTURE ISSUES

1. Molecular dipole manipulation at the nanoscale presents a broad horizon for further exploration. In particular, the formation of molecular dipole filaments as a spontaneous fluctuation effect as well as the possibility of having molecular dipole filaments of macroscopic length are exciting topics for both theoretical and experimental studies.
2. GER microfluidic logic gates open the possibility for integrated complex microfluidic circuitries to perform high-level smart functionalities.
3. An ideal GER fluid, with low zero field viscosity, yielding stresses in the range of 100 kPa, and showing no particle aggregation or sedimentation effect under long-term use, is still a challenge to be urgently addressed. Reaching such a goal can broaden GER fluids' application to actively controllable mechanical devices such as dampers, clutches, brakes, and locks.

DISCLOSURE STATEMENT

The authors are not aware of any biases that might be perceived as affecting the objectivity of this review.

ACKNOWLEDGMENTS

This work is supported by Hong Kong Research Grants Council grants RGC602207 and RGC621006. The authors also wish to thank Shuyu Chen for helpful assistance in the literature search and figure preparation.

LITERATURE CITED

- Agarwal AK, Yethiraj A. 2009. Low-density ordered phase in Brownian dipolar colloidal suspensions. *Phys. Rev. Lett.* 102:198301
- Ahn K, Agresti J, Chong H, Marquez M, Weitz DA. 2006. Electrocoalescence of drops synchronized by size-dependent flow in microfluidic channels. *Appl. Phys. Lett.* 88:264105
- Alexandre J, Tildesley DJ, Chapela GA. 1995. Molecular dynamics simulation of the orthobaric densities and surface tension of water. *J. Chem. Phys.* 102:4574–83
- Baroud CN, de Saint VMR, Delville JP. 2007. An optical toolbox for total control of droplet microfluidics. *Lab Chip* 7:1029–33
- Bergman DJ. 1978a. Analytical properties of the complex effective dielectric constant of a composite medium with applications to the derivation of rigorous bounds and to percolation problems. In *Electrical Transport and Optical Properties of Inhomogeneous Media*, ed. JC Garland, DB Tanner, pp. 46–61. Woodbury, NY: Am. Inst. Phys.
- Bergman DJ. 1978b. The dielectric constant of a composite material: a problem in classical physics. *Phys. Rep.* 43:377–407
- Bergman DJ. 1985. Bulk physical properties of composite media. In *Les methodes de l'homogenisation: theorie et applications en physique*, pp. 1–128. Paris: Eyrolles
- Bergman DJ, Stroud D. 1992. The physical properties of macroscopically inhomogeneous media. In *Solid State Physics*, vol. 46, ed. H Ehrenreich, F Seitz, D Turnbull, pp. 148–270. New York: Academic
- Bonnecaze RT, Brady JF. 1992a. Dynamic simulation of an electrorheological fluid. *J. Chem. Phys.* 96:2183–202
- Bonnecaze RT, Brady JF. 1992b. Yield stresses in electrorheological fluids. *J. Rheol.* 36:73–115

- Bossis G, Métayer C, Zubarev A. 2007. Analysis of chaining structures in colloidal suspensions subjected to an electric field. *Phys. Rev. E* 76:041401
- Bullough WA, ed. 1996. *Electrorheological Fluids, Magnetorheological Suspensions and Associated Technology: Proceedings of the 5th International Conference*. Singapore: World Sci.
- Chabert M, Viovy JL. 2008. Microfluidic high-throughput encapsulation and hydrodynamic self-sorting of single cells. *Proc. Natl. Acad. Sci. USA* 105:3191–96
- Chen SY, Huang X, van der Vegt N, Wen W, Sheng P. 2010. Giant electrorheological effect: a microscopic mechanism. *Phys. Rev. Lett.* 105:046001
- Chen TJ, Zitter RN, Tao R. 1992. Laser diffraction determination of the crystalline structure of an electrorheological fluid. *Phys. Rev. Lett.* 68:2555–58
- Chen Y, Conrad H. 1994. Electrostatic interactions for particle arrays in electrorheological fluids II: measurements. *Int. J. Mod. Phys. B* 8:2895–902
- Chen Y, Sprecher AE, Conrad H. 1991. Electrostatic particle-particle interactions in electrorheological fluids. *J. Appl. Phys.* 70:6796–803
- Cheng Y, Liu X, Guo J, Liu F, Li Z, et al. 2009. Fabrication of uniform core-shell structural calcium and titanium precipitation particles and enhanced electrorheological activities. *Nanotechnology* 20:055604
- Cheng Y, Wu K, Liu F, Guo J, Liu X, et al. 2010. Facile approach to large-scale synthesis of 1D calcium and titanium precipitate (CTP) with high electrorheological activity. *ACS Appl. Mater. Interfaces* 2:621–25
- Cheow LF, Yobas L, Kwong D. 2007. Digital microfluidics: droplet based logic gates. *Appl. Phys. Lett.* 90:054107
- Cho MS, Choi HJ, Ahn WS. 2004. Enhanced electrorheology of conducting polyaniline confined in MCM-41 channels. *Langmuir* 20:202–7
- Choi HJ, Cho MS, Kim JW, Kim CA, John MS. 2001. A yield stress scaling function for electrorheological fluids. *Appl. Phys. Lett.* 78:3806–8
- Choi HJ, Jhon MS. 2009. Electrorheology of polymers and nanocomposites. *Soft Matter* 5:1562–67
- Conrad H, Sprecher AF. 1994. Characteristics and mechanisms of electrorheological fluids. *J. Stat. Phys.* 64:1073–91
- Davis LC. 1992a. Finite-element analysis of particle-particle forces in electrorheological fluids. *Appl. Phys. Lett.* 60:319–21
- Davis LC. 1992b. Polarization forces and conductivity effects in electrorheological fluids. *J. Appl. Phys.* 72:1334–40
- Garstecki P, Fuerstman MJ, Whitesides GM. 2005. Oscillations with uniquely long periods in a microfluidic bubble generator. *Nat. Phys.* 1:168–71
- Gong X, Wu J, Huang X, Wen W, Sheng P. 2008. Influence of liquid phase on nanoparticle-based giant electrorheological fluid. *Nanotechnology* 19:165602
- Groisman A, Enzelberger M, Quake SR. 2003. Microfluidic memory and control devices. *Science* 300:955–58
- Gulley GL, Tao R. 1997. Structure of an electrorheological fluid. *Phys. Rev. E* 56:4328–36
- Halsey TC. 1992. Electrorheological fluids. *Science* 258:761–66
- Hass KC. 1993. Computer simulations of nonequilibrium structure formation in electrorheological fluids. *Phys. Rev. E* 47:3362–73
- Hu Y, Glass JL, Griffith AE, Fraden S. 1994. Observation and simulation of electrohydrodynamic instabilities in aqueous colloidal suspensions. *J. Chem. Phys.* 100:4674–82
- Huang X, Wen W, Yang S, Sheng P. 2006. Mechanisms of the giant electrorheological effect. *Solid State Commun.* 139:581–88
- Hynninen A-P, Dijkstra M. 2005. Phase diagram of dipolar hard and soft spheres: manipulation of colloidal crystal structures by an external field. *Phys. Rev. Lett.* 94:138303
- Indeikina PA, Chang HC. 2002. Electrokinetic displacement of air bubbles in microchannels. *Phys. Fluids* 14:1–14
- Ivlev AV, Morfill GE, Thomas HM, Rath C, Joyce G, et al. 2008. First observation of electrorheological plasmas. *Phys. Rev. Lett.* 100:095003
- Jeffries GDM, Kuo JS, Chiu DT. 2007. Dynamic modulation of chemical concentration in an aqueous droplet. *Angew. Chem. Int. Ed. Engl.* 46:1326–28

- Jensen K, Lee AP. 2004. Special issue foreword. *Lab Chip* 4:N31–32
- Joung J, Shen J, Grodzinski P. 2000. Micropumps based on alternating high-gradient magnetic fields. *IEEE Trans. Magn.* 36:2012–14
- Klingenberg DJ. 1993. Simulation of the dynamic oscillatory response of electrorheological suspensions: demonstration of a relaxation mechanism. *J. Rheol.* 37:199–215
- Klingenberg DJ, Swol FV, Zukoski CF. 1989. Dynamic simulation of electrorheological suspensions. *J. Chem. Phys.* 91:7888–95
- Klingenberg DJ, Swol FV, Zukoski CF. 1991a. The small shear rate response of electrorheological suspensions. I. Simulation in the point-dipole limit. *J. Chem. Phys.* 94:6160–69
- Klingenberg DJ, Swol FV, Zukoski CF. 1991b. The small shear rate response of electrorheological suspensions. II. Extension beyond the point-dipole limit. *J. Chem. Phys.* 94:6170–78
- Klingenberg DJ, Zukoski CZ, Hill JC. 1993. Kinetics of structure formation in electrorheological suspensions. *J. Appl. Phys.* 73:4644–48
- Lee ME, van der Vegt NFA. 2006. Does urea denature hydrophobic interactions? *J. Am. Chem. Soc.* 128:4948–49
- Liau A, Karnik R, Majumdar A, Cate JH. 2005. Mixing crowded biological solutions in milliseconds. *Anal. Chem.* 77:7618–25
- Link DR, Grasland-Mongrain E, Duri A, Sarrazin F, Cheng Z, et al. 2006. Electric control of droplets in microfluidic devices. *Angew. Chem. Int. Ed. Engl.* 45:2556–60
- Liu K, Ding H, Chen Y, Zhao XZ. 2007. Droplet-based synthetic method using microflow. *Microfluid. Nanofluid.* 3:239–43
- Liu L, Chen X, Niu X, Wen W, Sheng P. 2006a. Electrorheological fluid-actuated microfluidic pump. *Appl. Phys. Lett.* 89:083505
- Liu L, Niu X, Wen W, Sheng P. 2006b. Electrorheological fluid-actuated flexible platform. *Appl. Phys. Lett.* 88:173505
- Lu Y, Shen R, Wang XZ, Sun G, Lu KQ. 2009. The synthesis and electrorheological effect of a strontium titanyl oxalate suspension. *Smart Mater. Struct.* 18:025012
- Luo Y, Zhang Q, Qin J, Lin B. 2007. Further improvement of hydrostatic pressure sample injection for microchip electrophoresis. *Electrophoresis* 28:4769–71
- Ma H, Wen W, Tam WY, Sheng P. 2003. Dielectric electrorheological fluids: theory and experiments. *Adv. Phys.* 52:343–83
- Ma HR, Wen W, Tam WY, Sheng P. 1996. Frequency dependent electrorheological properties: origin and bounds. *Phys. Rev. Lett.* 77:2499–502
- Manz A, Graber N, Widmer HM. 1990. Miniaturized total chemical analysis systems: a novel concept for chemical sensing. *Sens. Actuators B* 1:244–48
- Mazouchi A, Homsy GM. 2001. Thermocapillary migration of long bubbles in polygonal tubes. *Phys. Fluids* 13:1594–600
- Milton GW. 1979. Theoretical studies of the transport properties of inhomogeneous media. *Rep. TP /79/1*, Univ. Sydney, Austr.
- Milton GW. 1981a. Bounds on the complex permittivity of a two-component composite material. *J. Appl. Phys.* 52:5286–93
- Milton GW. 1981b. Bounds on the transport and optical properties of a two-component composite material. *J. Appl. Phys.* 52:5294–304
- Milton GW. 2002. *The Theory of Composites*. Cambridge, UK: Cambridge Univ. Press
- Mosadegh B, Kuo C, Tung Y, Torisawa Y, Bersano-Begey T, et al. 2010. Integrated elastomeric components for autonomous regulation of sequential and oscillatory flow switching in microfluidic devices. *Nat. Phys.* 6:433–37
- Mountain RD, Thirumalai D. 2004. Importance of excluded volume on the solvation of urea in water. *J. Phys. Chem. B* 108:6826–31
- Nakano M, Katou T, Satou A, Miyata K, Matsushita K. 2002. Three-ports micro ER valve for ER suspension fabricated by photolithography. *J. Intell. Mater. Syst. Struct.* 13:503–8
- Niu X, Liu L, Wen W, Sheng P. 2006a. Active microfluidic mixer chip. *Appl. Phys. Lett.* 88:153508

- Niu X, Liu L, Wen W, Sheng P. 2006b. Hybrid approach to high-frequency microfluidic mixing. *Phys. Rev. Lett.* 97:044501
- Niu X, Wen W, Lee Y. 2005. Electrorheological-fluid-based microvalve. *Appl. Phys. Lett.* 87:243501
- Niu X, Zhang M, Peng S, Wen W, Sheng P. 2007. Real-time detection, control and sorting of microfluidic droplets. *Biomicrofluidics* 1:044101-12
- Niu X, Zhang M, Wu J, Wen W, Sheng P. 2009. Generation and manipulation of “smart” droplets. *Soft Matter* 5:576-81
- Paik P, Pamula VK, Pollack MG, Fair RB. 2003. Electrowetting-based droplet mixers for microfluidic systems. *Lab Chip* 3:28-33
- Pollack MG, Shenderov AD, Fair RB. 2002. Electrowetting-based actuation of droplets for integrated microfluidics. *Lab Chip* 2:96-101
- Prakash M, Gershenfeld N. 2007. Microfluidic bubble logic. *Science* 315:832-35
- Priest C, Herminghaus S, Seemann R. 2006. Controlled electrocoalescence in microfluidics: targeting a single lamella. *Appl. Phys. Lett.* 89:134101
- Psaltis D, Quake SR, Yang C. 2006. Developing optofluidic technology through the fusion of microfluidics and optics. *Nature* 442:381-86
- Ren H, Srinivasan V, Fair RB. 2003. Automated electrowetting-based droplet dispensing with good reproducibility. *Proc. μ TAS 2003 7th Int. Conf. Micro Total Anal. Syst.*, ed. MA Northrup, KF Jensen, DJ Harrison, pp. 993-96. Cleveland Heights, OH: Transducers Res. Found.
- Rhee M, Burns MA. 2009. Microfluidic pneumatic logic circuits and digital pneumatic microprocessors for integrated microfluidic systems. *Lab Chip* 9:3131-43
- Schwartz A, Vykoukal JV, Gascoyne PRC. 2004. Droplet-based chemistry on a programmable micro-chip. *Lab Chip* 4:11-17
- Shen M, Cao JG, Xue HT, Huang JP, Zhou LW. 2006. Structure of polydisperse electrorheological fluids: experiment and theory. *Chem. Phys. Lett.* 423:165-69
- Shen R, Wang X, Lu Y, Wang D, Sun G, et al. 2009. Polar-molecule-dominated electrorheological fluids featuring high yield stresses. *Adv. Mater.* 21:4631-35
- Sheng P, Wen W. 2010. Electrorheology: statics and dynamics. *Solid State Commun.* 150:1023-39
- Shih YH, Sprecher AE, Conrad H. 1994. Electrostatic interactions for particle arrays in electrorheological fluids I: calculations. *Int. J. Mod. Phys. B* 8:2877-94
- Sides SW, Curro J, Grest GS, Stevens MJ, Soddemann T, et al. 2002. Structure of poly(dimethylsiloxane) melts: theory, simulation and experiment. *Macromolecules* 35:6455-65
- Sun H, Yu KW. 2003. Ground state of a polydisperse electrorheological solid: beyond the dipole approximation. *Phys. Rev. E* 67:011506
- Tam WY, Yi GH, Wen W, Ma HR, Loy MMT, Sheng P. 1997. New electrorheological fluids: theory and experiment. *Phys. Rev. Lett.* 78:2987-90
- Tan P, Tian WJ, Wu XF, Huang JY, Zhou LW, Huang JP. 2009. Saturated orientational polarization of polar molecules in giant electrorheological fluids. *J. Phys. Chem. B* 113:9092-97
- Tan YC, Ho YL, Lee AP. 2007. Droplet coalescence by geometrically mediated flow in microfluidic channels. *Microfluid. Nanofluid.* 3:495-99
- Tan YC, Ho YL, Lee AP. 2008. Microfluidic sorting of droplets by size. *Microfluid. Nanofluid.* 4:343-48
- Tang X, Wu C, Conrad H. 1995a. On the conductivity model for the electrorheological effect. *J. Rheol.* 39:1059-74
- Tang X, Wu C, Conrad H. 1995b. On the conductivity model for the electrorheological response of dielectric particles with a conducting film. *J. Appl. Phys.* 78:4183-88
- Tao R, Jiang Q. 1994. Simulation of structure formation in an electrorheological fluid. *Phys. Rev. Lett.* 73:205-8
- Tao R, Sun JM. 1991. Three-dimensional structure of induced electrorheological solid. *Phys. Rev. Lett.* 67:398-401
- van der Vegt NFA, Lee ME, Trzesniak D, van Gunsteren WF. 2006. Enthalpy-entropy compensation in the effects of urea on hydrophobic interactions. *J. Phys. Chem. B* 110:12852-55
- Wang BX, Zhao XP, Zhao Y, Ding CL. 2007. Titanium oxide nanoparticle modified with chromium ion and its giant electrorheological activity. *Compos. Sci. Technol.* 67:3031-38

- Wang L, Zhang M, Li J, Gong X, Wen W. 2010. Logic control of microfluidics with smart colloid. *Lab Chip* 10:2869–74
- Wang ZW, Fang HP, Lin ZF, Zhou LW. 2000. Simulation of field-induced structural formation and transition in electromagnetorheological suspensions. *Phys. Rev. E* 61:6837–44
- Wang ZW, Lin ZF, Tao RB. 1996. Many-body effect in electrorheological responses. *Int. J. Mod. Phys. B* 10:1153–66
- Weaver JA, Melin J, Stark D, Quake SR, Horowitz MA. 2010. Static control logic for microfluidic devices using pressure-gain valves. *Nat. Phys.* 6:218–23
- Wen W, Huang X, Sheng P. 2004. Particle size scaling of the giant electrorheological effect. *Appl. Phys. Lett.* 85:299–301
- Wen W, Huang X, Sheng P. 2007. Electrorheological fluids: structures and mechanisms. *Soft Matter* 4:200–10
- Wen W, Huang X, Yang S, Lu K, Sheng P. 2003. The giant electrorheological effect in suspensions of nanoparticles. *Nat. Mater.* 2:727–30
- Wen W, Wang N, Ma HR, Lin ZF, Tam WY, et al. 1999. Field induced structural transition in mesocrystals. *Phys. Rev. Lett.* 82:4248–51
- Winslow WM. 1949. Induced fibrillation of suspensions. *J. Appl. Phys.* 20:1137–40
- Yethiraj A, van Blaaderen A. 2003. A colloidal model system with an interaction tunable from hard sphere to soft and dipolar. *Nature* 421:513–17
- Yin JB, Zhao XP. 2004. Giant electrorheological activity of high surface area mesoporous cerium-doped TiO₂ templated by block copolymer. *Chem. Phys. Lett.* 398:393–99
- Yoshida K, Kikuchi M, Park J, Yokota S. 2002. Fabrication of micro electro-rheological valves (ER valves) by micromachining and experiments. *Sens. Actuators A* 95:227–33
- Zhan W, Crooks RM. 2003. Microelectrochemical logic circuits. *J. Am. Chem. Soc.* 125:9934–35
- Zhang J, Gong X, Liu C, Wen W, Sheng P. 2008a. Electrorheological fluid dynamics. *Phys. Rev. Lett.* 101:194503
- Zhang M, Gong X, Wen W. 2009. Manipulation of microfluidic droplets by electrorheological fluid. *Electrophoresis* 30:3116–23
- Zhang M, Wu J, Niu X, Wen W, Sheng P. 2008b. Manipulations of microfluidic droplets using electrorheological carrier fluid. *Phys. Rev. E* 78:066305
- Zhu X, Gao C, Choi JW, Bishop PL, Ahn CH. 2005. On-chip generated mercury microelectrode for heavy metal ion detection. *Lab Chip* 5:212–17



Contents

Aeroacoustics of Musical Instruments <i>Benoit Fabre, Joël Gilbert, Avraham Hirschberg, and Xavier Pelorson</i>	1
Cascades in Wall-Bounded Turbulence <i>Javier Jiménez</i>	27
Large-Eddy-Simulation Tools for Multiphase Flows <i>Rodney O. Fox</i>	47
Hydrodynamic Techniques to Enhance Membrane Filtration <i>Michel Y. Jaffrin</i>	77
Wake-Induced Oscillatory Paths of Bodies Freely Rising or Falling in Fluids <i>Patricia Ern, Frédéric Risso, David Fabre, and Jacques Magnaudet</i>	97
Flow and Transport in Regions with Aquatic Vegetation <i>Heidi M. Nepf</i>	123
Electrorheological Fluids: Mechanisms, Dynamics, and Microfluidics Applications <i>Ping Sheng and Weijia Wen</i>	143
The Gyrokinetic Description of Microturbulence in Magnetized Plasmas <i>John A. Krommes</i>	175
The Significance of Simple Invariant Solutions in Turbulent Flows <i>Genta Kawahara, Markus Uhlmann, and Lennaert van Veen</i>	203
Modern Challenges Facing Turbomachinery Aeroacoustics <i>Nigel Peake and Anthony B. Parry</i>	227
Liquid Rope Coiling <i>Neil M. Ribe, Mehdi Habibi, and Daniel Bonn</i>	249
Dynamics of the Tear Film <i>Richard J. Braun</i>	267
Physics and Computation of Aero-Optics <i>Meng Wang, Ali Mani, and Stanislav Gordeyev</i>	299

Smoothed Particle Hydrodynamics and Its Diverse Applications <i>J. J. Monaghan</i>	323
Fluid Mechanics of the Eye <i>Jennifer H. Siggers and C. Ross Ethier</i>	347
Fluid Mechanics of Planktonic Microorganisms <i>Jeffrey S. Guasto, Roberto Rusconi, and Roman Stocker</i>	373
Nanoscale Electrokinetics and Microvortices: How Microhydrodynamics Affects Nanofluidic Ion Flux <i>Hsueh-Chia Chang, Gilad Yossifon, and Evgeny A. Demekhin</i>	401
Two-Dimensional Turbulence <i>Guido Boffetta and Robert E. Ecke</i>	427
“Vegetable Dynamics”: The Role of Water in Plant Movements <i>Jacques Dumais and Yoël Forterre</i>	453
The Wind in the Willows: Flows in Forest Canopies in Complex Terrain <i>Stephen E. Belcher, Ian N. Harman, and John J. Finnigan</i>	479
Multidisciplinary Optimization with Applications to Sonic-Boom Minimization <i>Juan J. Alonso and Michael R. Colonno</i>	505
Direct Numerical Simulation on the Receptivity, Instability, and Transition of Hypersonic Boundary Layers <i>Xiaolin Zhong and Xiaowen Wang</i>	527
Air-Entrainment Mechanisms in Plunging Jets and Breaking Waves <i>Kenneth T. Kiger and James H. Duncan</i>	563
Indexes	
Cumulative Index of Contributing Authors, Volumes 1–44	597
Cumulative Index of Chapter Titles, Volumes 1–44	606

Errata

An online log of corrections to *Annual Review of Fluid Mechanics* articles may be found at <http://fluid.annualreviews.org/errata.shtml>